Electron dynamics in inhomogeneous magnetic fields

2010 J. Phys.: Condens. Matter 22 253201

(http://iopscience.iop.org/0953-8984/22/25/253201)

IOP Publishing Journal of Physics: Condensed Matter

J. Phys.: Condens. Matter **22** (2010) 253201 (28pp) doi:10.1088/0953-8984/22/25/253201

TOPICAL REVIEW

Electron dynamics in inhomogeneous magnetic fields

Alain Nogaret

Department of Physics, University of Bath, Bath BA2 7AY, UK

E-mail: A.R.Nogaret@bath.ac.uk

Received 14 April 2010
Published 4 June 2010
Online at stacks.iop.org/JPhysCM/22/253201

Abstract

This review explores the dynamics of two-dimensional electrons in magnetic potentials that vary on scales smaller than the mean free path. The physics of microscopically inhomogeneous magnetic fields relates to important fundamental problems in the fractional quantum Hall effect, superconductivity, spintronics and graphene physics and spins out promising applications which will be described here. After introducing the initial work done on electron localization in random magnetic fields, the experimental methods for fabricating magnetic potentials are presented. Drift–diffusion phenomena are then described, which include commensurability oscillations, magnetic channelling, resistance resonance effects and magnetic dots. We then review quantum phenomena in magnetic potentials including magnetic quantum wires, magnetic minibands in superlattices, rectification by snake states, quantum tunnelling and Klein tunnelling. The third part is devoted to spintronics in inhomogeneous magnetic fields. This covers spin filtering by magnetic field gradients and circular magnetic fields, electrically induced spin resonance, spin resonance fluorescence and coherent spin manipulation.

(Some figures in this article are in colour only in the electronic version)

Contents

1. Introduction

The use of spatially varying magnetic fields can be traced back to the measurement of the magnetic moment of silver atoms by Stern and Gerlach. Their experimental set-up used an electromagnet fitted with asymmetric pole pieces to produce

a macroscopic magnetic field gradient varying over distances of centimetres. Conversely, magnetic fields that vary on atomic scales are obtained with magnetic impurities. The action of magnetic impurities is studied within the Kondo effect. The study of magnetic fields varying on the scale of the electron mean free path is an active field of research that has developed over the past decade. This is in part because recent technological advances have allowed the fabrication of nanomagnets with well defined shapes and because of progress in the growth of high mobility two-dimensional electron gases (2DEGs). The impetus for the study of magnetically modulated 2DEGs arose from the problem of electron localization in a *random magnetic field*. The question is to determine whether the wavefunction of 2D electrons is localized or extended in the presence of a random magnetic field with zero average. The problem is closely related to weak localization in *random electrostatic potentials*. Electrostatic disorder is known to localize the electron wavefunctions in two dimensions making the 2DEG an insulator at 0 K. Applying a homogeneous magnetic field (B) to the 2DEG has the effect of breaking the time reversal symmetry of clockwise and anticlockwise interference paths. When Landau levels form, all electronic states remain localized except for a narrow band at the centre where metallic conduction takes place. A random magnetic field with zero average breaks time reversal symmetry locally and randomly. The disruption of extended states by the random potential *a priori* provides a good reason to expect electron localization and an insulating behaviour in the random magnetic field [1–3]. Zhang and Arovas [4] however pointed to the existence of magnetic edge states at the boundaries between positive and negative magnetic field domains [5]. These states tunnel through saddle points of the random magnetic potential and percolate through nodes of the network to form globally extended states. Hence, it appears that the 2DEG modulated by a random magnetic field is in fact a metal, a result supported by numerical simulations [6–9].

Quantum transport in quasi-random magnetic fields has been investigated experimentally when the correlation length of magnetic fluctuations is larger than the electron mean free path [10]. The experiment thus departs from the theoretical scenario considered above. Instead, the 2DEG behaves as a network of diffusive magnetic domains with their own local Hall resistivity. In this case, theory predicts a V-shaped magnetoresistance $\rho_{xx} \propto |B|$ [11], which is confirmed experimentally [10]. Magnetic field profiles varying on scales smaller than the mean free path were first produced by patterning type II superconductors on top of 2DEGs [12]. In this case, the vortex lattice threads the 2DEG with a hexagonal array of magnetic spots separated by 50 nm/$[B(T)]^{1/2}$ (Al films). Small angle deflection of ballistic electrons by the magnetic spots gives a positive magnetoresistance. Electron diffraction is observed when the wavelength of Fermi electrons is tuned to the spacing between vortices. Geim *et al* [13] demonstrated this effect by detecting a maximum correction to the Hall resistance under diffraction conditions. Over the past decade and a half, magnetic field profiles of high amplitude and zero average have been obtained. The electron and electron spin dynamics in these potentials will be reviewed here. The paper will provide several examples of the importance of magnetic edge states for both fundamental physics and applications. It describes milestone results from the first demonstration of lateral magnetic superlattices to the coherent control of the electron spin.

The review is organized as follows. Section 1 introduces the problem which motivated the study of magnetically modulated 2DEGs; section 2 reviews the experimental methods used for applying magnetic modulations to 2DEGs; section 3 describes semiclassical transport anomalies due to drift–diffusion processes; section 4 focuses on quantum mechanical properties; section 5 reveals the advantages of using fringing magnetic fields for manipulating the electron spin and in particular the possibility of activating spin resonance by driving a direct current through a magnetically modulated 2DEG. Section 6 discusses prospects and applications.

2. Experimental strategies for making inhomogeneous magnetic fields

2.1. Micromagnetic and superconducting elements

One way to obtain a microscopically inhomogeneous magnetic field is to fabricate *micromagnets* in the proximity of a 2DEG. The stray magnetic field applies a local Lorentz force that deflects ballistic electrons. The magnetic modulation profile can be calculated to an excellent degree of accuracy [14] provided the magnetization M is homogeneous. Uniform magnetization is obtained by using hard uniaxial magnets such as $SmCo_5$ or by saturating the magnetization with an external magnetic field. The dimensions of micromagnets are otherwise measured to a high degree of accuracy from AFM imaging. The thickness of the buffer layer separating the 2DEG from the micromagnet is known to within an atomic monolayer. These data allow the stray magnetic field at the site of the 2DEG to be calculated accurately. Consider for instance the one-dimensional magnetic superlattice shown in figure 1(a). The grating of cobalt finger gates modulates the GaAs/AlGaAs heterojunction set a distance z_0 beneath the surface. The stray magnetic field emanating from a periodic array is easily obtained from Fourier transformation of Maxwell's equations [15, 16]. One obtains

$$\begin{aligned} B_{1,x}(x, z_0) &= \mu_0 M \frac{hd}{a} \sum_{n=1}^{\infty} q_n F(q_n) \mathrm{e}^{-q_n(z_0+h/2)} \sin(q_n x - \theta), \\ B_{1,y}(x, z_0) &= 0, \\ B_{1,z}(x, z_0) &= \mu_0 M \frac{hd}{a} \sum_{n=1}^{\infty} q_n F(q_n) \mathrm{e}^{-q_n(z_0+h/2)} \cos(q_n x - \theta), \end{aligned} \tag{1}$$

where $q_n = 2\pi n/a$, a is the period of the array, h the height of the cobalt fingers and d their width, θ is the tilt angle of the magnetization and

$$F(q_n) = \frac{\sin(q_n d/2)}{(q_n d/2)} \frac{\sinh(q_n h/2)}{(q_n h/2)}, \tag{2}$$

is the form factor of rectangular stripes. Since electron motion is confined to the plane, magnetoresistive effects will only

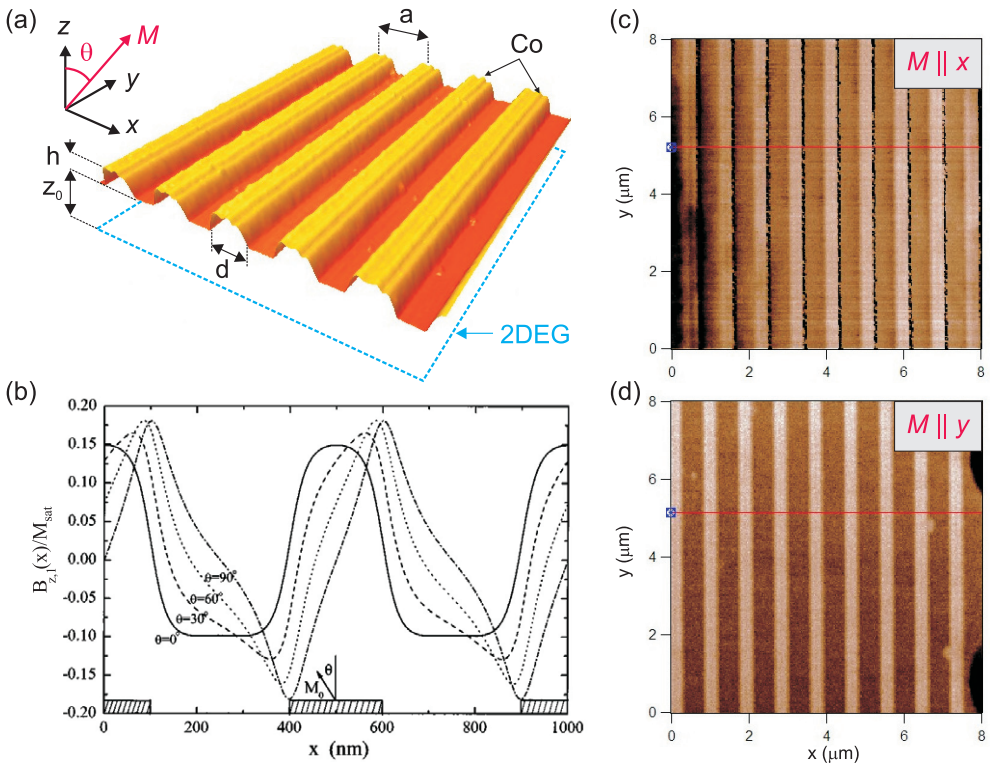

Figure 1. (a) Cobalt finger gates at the surface of a 2DEG. (b) Magnetic modulation profiles at different tilt angles of the magnetization. (c) MFM image of the cobalt grating magnetized along the short axis of the stripes, in the plane of the 2DEG. The magnetic poles appear as the black lines. (d) MFM image of the grating magnetized along the long axis. The magnetic poles are absent. Parameters: $a = 400$ nm, $d = 200$ nm, $h = 160$ nm and $z_0 = 90$ nm.

depend on the perpendicular magnetic field component, $B_{1,z}$, which is plotted in figure 1(b). When the magnetization rotates from normal to in-plane ($\parallel x$), the magnetic field modulation changes from rectangular to triangular shape. At saturation, the magnetization of cobalt is $\mu_0 M_s = 1.82$ T, which gives a modulation amplitude of ± 0.3 T. The magnetic modulation can be switched off by magnetizing the grating in the y-direction. This device is very useful to the experimentalist for demonstrating the effects of the magnetic modulation. The MFM images of the grating are displayed in panels (c) and (d) when the magnetization is respectively along the short axis and the long axis of the stripes. Note that the formation of magnetic poles in the former case corresponds to the situation where a magnetic modulation is applied.

Superconducting elements may also be used to screen the applied magnetic field using the Meissner effect. The screening mechanism is however complicated by the fact that most type I superconductors, such as lead, exhibit type II superconductivity when laid in thin films. Below the first critical field, B_{c1}, the superconducting element is a perfect diamagnet with magnetization given by $\mu_0 M = -B$. The stray magnetic field emanating from a 1D superconducting grating is obtained by substituting $\mu_0 M$ with $-B$ in equations (1). Between the first and the second critical field, vortex lines penetrate from the edges of the superconductor to weaken the modulation. The strength of the magnetic modulation decreases with increasing B until it vanishes at B_{c2}. When $B_{c1} < B < B_{c2}$ the pinning of vortices plays a crucial role as the sign of magnetic modulation depends on whether the external magnetic field is ramped up or down. When the magnetic field is ramped down, the flux lines pinned inside the superconductor cannot easily migrate outside. Conversely, when the magnetic field is ramped up the flux lines cannot easily penetrate inside. The pinning of vortices is responsible for a change in the phase of the magnetic modulation by π between sweep up and sweep down.

The generation of fringing magnetic fields by driving a current through a metal stripline has been considered theoretically [18] and is implemented in MRAM technology. It is however not an effective way of producing inhomogeneous magnetic fields because semiconductor heterojunctions impose a buffer layer between the stripline and the 2DEG, over which the stray magnetic field decays to negligible levels.

Magnetic modulations produced by the above methods are generally accompanied by parasitic electrostatic modulations. These arise from the build-up of strain at the metal–semiconductor interface as the sample is cooled down to cryogenic temperatures. Polar semiconductors such as GaAs develop a piezoelectric potential of the order of the millivolt. Magnetostriction in the ferromagnet may also modify the piezoelectric potential to the extent where the magnetization curve becomes detectable by voltage measurements alone. This effect is shown in figure 2, where a 2D hole gas is modulated by a dysprosium stripe. The piezo-voltage exhibits a hysteresis curve at 1.7 K that resembles the magnetization curve of dysprosium. The thermal activation of holes at

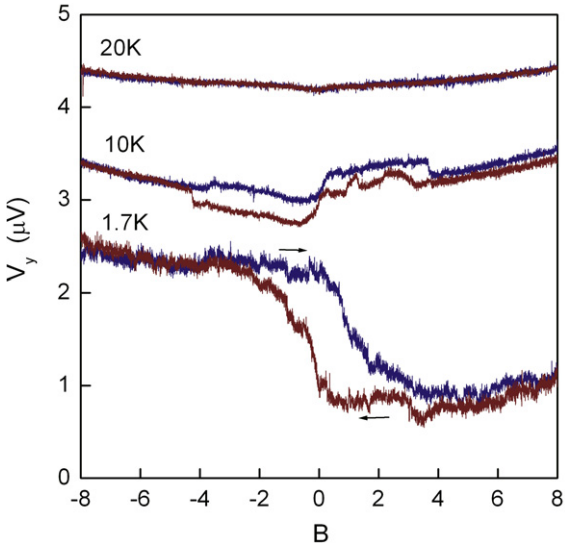

Figure 2. The piezo-magnetostrictive effect. A finite piezoelectric voltage is measured across a 2D hole gas modulated by a dysprosium finger gate. The stripe, at the centre of the Hall bar, applies variable strain to the semiconductor through magnetostriction. The magnetization curve of dysprosium is detected in the piezo-voltage. No current is applied. The finger gate is magnetized along its short axis and in the plane.

20 K is sufficient to screen the piezoelectric potential causing the hysteresis curve to vanish. Taking the magnetostrictive constant of dysprosium as $\varepsilon_y = 10.6 \times 10^{-3}$ and the valence band deformation potential as $\Xi = 2.7$ eV, the maximum piezo-voltage is $V_y = 1.6$ mV. The residual electrostatic modulation may be attenuated by aligning stripes with the [100] crystallographic axes or by equalizing the distribution of strain with a metal gate.

2.2. *Non-planar two-dimensional electron gases*

An alternative method to obtain magnetic steps is to overgrow GaAs/AlGaAs heterojunctions on non-planar substrates [19–21]. The Hall bar in figure 3(a) incorporates an etched facet on which the 2DEG was re-grown. The magnetic modulation being the vector component perpendicular to the 2DEG, an external magnetic field applied in the plane will give a modulation field which is finite in the facet and zero elsewhere. Mendach *et al* [22] have extended this idea to cylindrical 2DEGs—see figures 3(b)–(d). They have micromachined a free standing 2DEG and rolled it up around a cylinder to obtain a sinusoidal modulation. The electronic band structure corresponding to this geometry has been calculated by Foden *et al* [23]. Non-planar structures are attractive for making arbitrarily large magnetic modulations.

2.3. *Chern–Simons effective magnetic field*

In the fractional quantum Hall effect near filling factor $\nu = 1/2$, the system of strongly correlated electrons is equivalent to non-interacting composite fermions with a well defined Fermi surface. A composite fermion consists of an electron paired with two flux quanta which oppose the applied magnetic field.

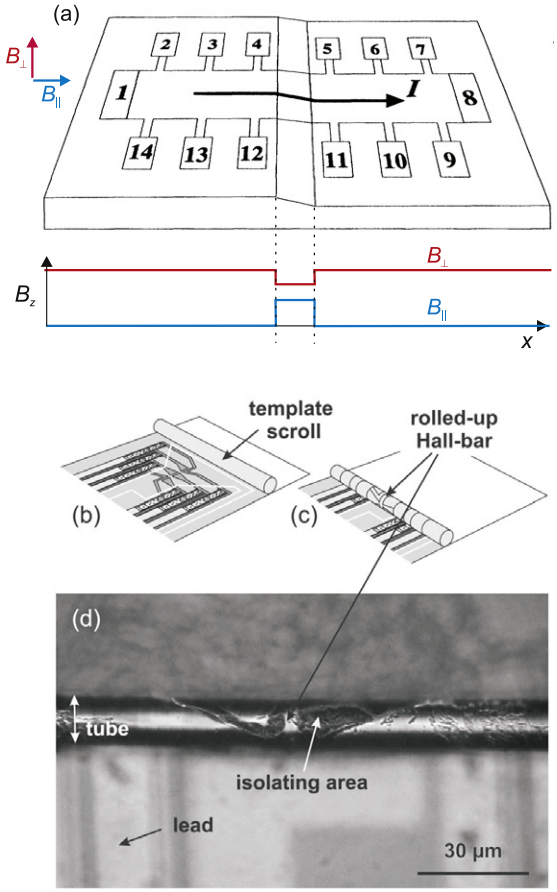

Figure 3. Inhomogeneous magnetic fields in non-planar 2DEGs: (a) GaAs/AlGaAs heterojunction grown on a step etch and fabricated as a Hall bar; (b)–(d) micromachined and rolled-up Hall bars. Reproduced with permission from [22]. Copyright 2006, American Institute of Physics.

The net effective field experienced by composite fermions is $B_{\text{eff}} = (1 - 2\nu)B$. Since ν depends on the local electron concentration $n_s(x)$ through $\nu(x) = n_s(x)(h/eB)$, the spatial modulation of the electron concentration is equivalent to a spatial modulation of the effective magnetic field. The observation of both commensurability oscillations [24] and the channelling of composite fermions in snake orbits [25] have given direct evidence for the effective modulation field.

3. Drift–diffusion transport phenomena

Now consider the magnetic superlattice of figure 1. The electron mean free path $l \simeq 10$ μm is larger than the period of the magnetic field $a = 400$ nm. This makes transport ballistic on the scale of about 20 superlattice periods. While the local magnetic field bends electron trajectories, it imparts a drifting motion in the direction perpendicular to the gradient of magnetic field. This motion depends on initial conditions since transport is ballistic. Resistance measurements by contrast are performed with voltage probe spacings larger than the mean free path. The measurement averages the drift motion over the entire set of initial conditions, thus probing the diffusive

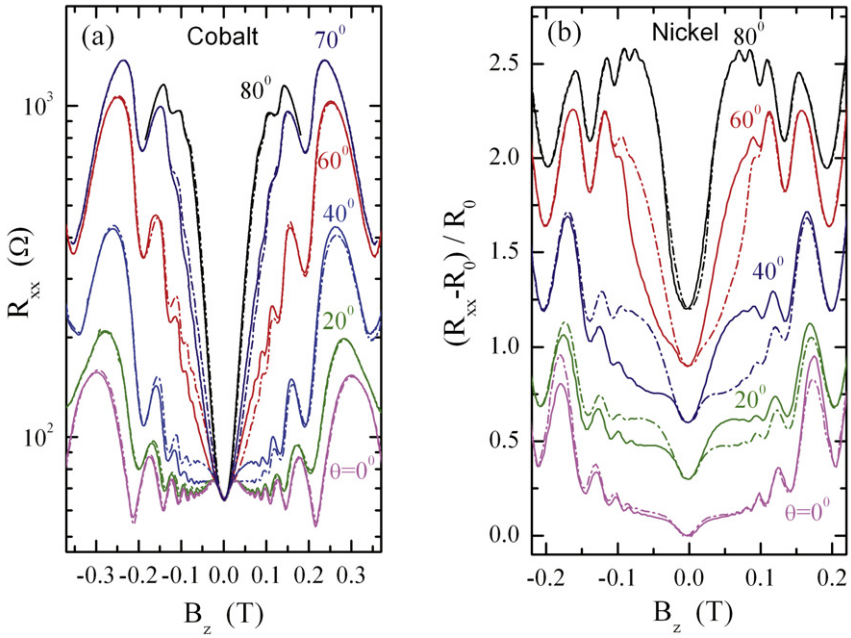

Figure 4. Magnetoresistance of (a) cobalt and (b) nickel superlattices as a function of the perpendicular component of the applied magnetic field, $B\cos\theta$: up sweep (full lines), down sweep (dash–dotted lines). The applied magnetic field is tilted by θ with respect to the normal to the 2DEG. Parameters: $a = 400$ nm, $d = 200$ nm, $h = 160$ nm, $z_0 = 35$ nm. The stripes are aligned with the [100] crystallographic axis, i.e. at 45° from the cleaving edge of the (001) wafer.

regime. This section reports on drift–diffusion phenomena in inhomogeneous magnetic fields.

3.1. Commensurability oscillations in the magnetoresistance

Commensurability oscillations in the magnetoresistance are observed when the amplitude of the periodic magnetic modulation $\tilde{B}_1$ is weaker than the external magnetic field, namely $\tilde{B}_1 < B$. The total magnetic field $B + B_{1,z}(x)$ does not change sign. The commensurability oscillations of cobalt and nickel superlattices are shown in figure 4 at $\theta = 0°$. These oscillations originate in the periodic enhancement of the drift velocity of the cyclotron guiding centre. To understand this, consider a cyclotron orbit of radius $R_c = \hbar k_F/(eB)$ on the Fermi surface ($k_F = \sqrt{2\pi n_s}$). The effect of the periodic magnetic field is mostly felt at the edges of the orbit where the electron spends a large amount of time in one magnetic domain. When magnetic domains at the opposite edges of the orbit have equal magnetic field, the cyclotron orbit is closed and stationary. Otherwise, a difference in curvature radii appears which sets the guiding centre of the orbit in motion. Ramping up the external magnetic field reduces R_c and induces oscillations of the diffusion coefficient δD_{yy}. These oscillations are periodic in B^{-1} like Shubnikov–de Haas oscillations, but are essentially classical phenomena. The maxima in δD_{yy} correspond to maxima in ρ_{xx}. This prosaically means that while an electron spends time drifting sideways, the longitudinal resistance is high. Note that the periodic modulation does not modify the ρ_{xy} component. This is because an equal number of cyclotron orbits drift along $y > 0$ and $y < 0$. The averaging over all initial conditions means that there is no net additional charge on the Hall probes. This effect is also responsible for the absence of commensurability oscillations in ρ_{yy}. The anisotropy in the diagonal components of the resistivity tensor is one important difference between the commensurability oscillations and the Shubnikov–de Haas effect.

Magnetic commensurability oscillations were first observed with 1D superconducting gratings [26], dysprosium gratings [28] and nickel gratings [29]. The theory of the oscillatory magnetoresistance was developed by Peeters and Vasilopoulos [30] and Gerhardts [15] to extend the semiclassical results of Beenakker [31] to magnetic modulations. When a periodic magnetic field $B_{1,z}(x) = \tilde{B}_1\cos(2\pi x/a)$ is applied in phase with an electrostatic potential $V(x) = V_1\cos(2\pi x/a)$, the magnetoresistance is given by [30]

$$\frac{R_{xx} - R_0}{R_0} = \left[\frac{ak_F}{4\pi^2}\left(\frac{\hbar\omega_1}{E_F}\right)^2\left(\frac{l}{r_c}\right)^2 + \left(\frac{V_1}{E_F}\right)^2\left(\frac{l^2}{aR_c}\right)\right] \times \left[1 - \frac{T/T_a}{\sinh(T/T_a)} + \frac{T/T_a}{\sinh(T/T_a)} \times \sin^2\left(\frac{2\pi R_c}{a} - \frac{\pi}{4} + \phi\right)\right], \quad (3)$$

where l is the elastic mean free path, $r_c = (\hbar/eB)^{1/2}$ is the magnetic length, $\omega_1 = e\tilde{B}_1/m^*$, $\omega_c = eB/m^*$, m^* is the electron effective mass, k_F and E_F are the Fermi wavevector and Fermi energy, $R_c = \hbar k_F/eB$ and $4\pi^2 k_B T_a = \hbar\omega_c a k_F$. The phase of the commensurability oscillations is given by

$$\tan\phi = 2\pi V_1/(ak_F\hbar\omega_1). \quad (4)$$

The first term in the left bracket of equation (3) is the amplitude of the magnetic commensurability oscillations whereas the second term relates to the electrostatic commensurability

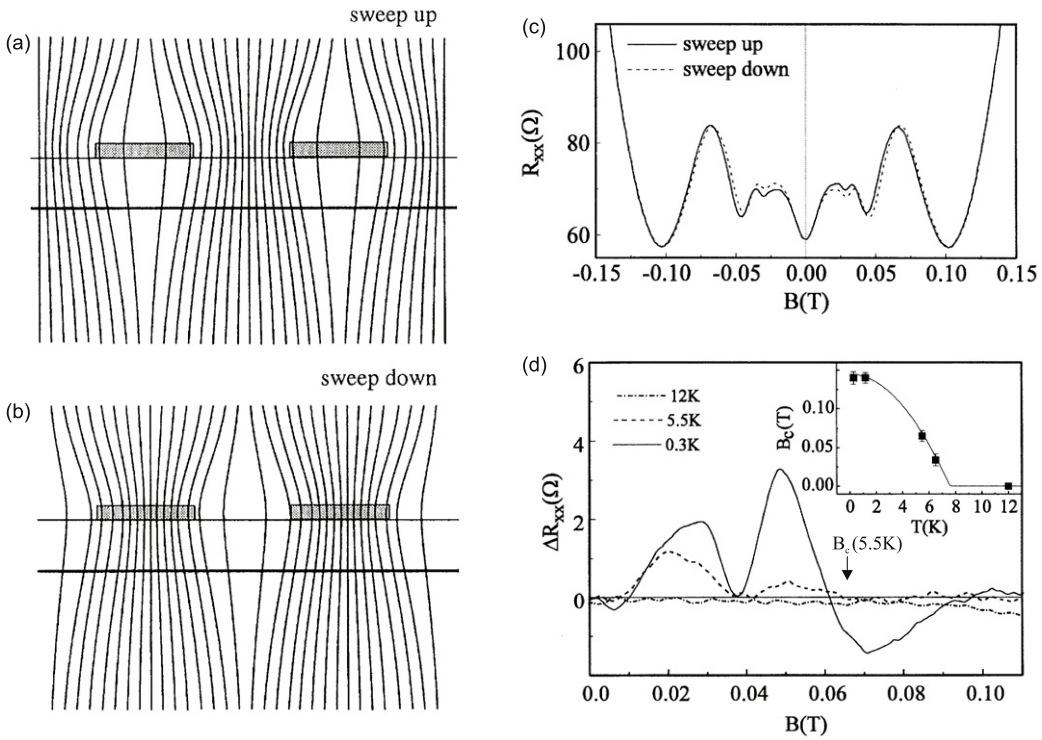

Figure 5. (a), (b) Magnetic flux pinning mechanism in a superconducting (Pb) grating. The Pb stripes screen the magnetic field on the way up (a) and trap flux lines on the sweep down (b). The phase of the magnetic modulation changes by π between sweep up and sweep down. (c) Magnetoresistance when B is swept up and down; (d) magnetic commensurability oscillations are seen in the difference between the sweep up and sweep down curves. The oscillations vanish above the critical temperature of Pb (7 K). Inset: temperature dependence of the cut-off magnetic field B_c. Parameters: $a = 2\ \mu$m, $d = 1\ \mu$m, $h = 200$ nm, $z_0 = 650$ nm. Reproduced with permission from [26]. Copyright 1995 by the American Physical Society.

oscillations. In the ballistic regime, l/r_c is much larger than one. This explains why magnetic commensurability oscillations can be observed despite the small amplitude of the magnetic potential ($\hbar\omega_1 \ll E_F$). The second square brackets include the oscillatory term due to the guiding centre drift. The phase of the oscillations varies between $\phi = +\pi/2$ for a pure electrostatic modulation and $\phi = 0$ for a pure magnetic modulation. This phase is determined by plotting the index of oscillation minima i as a function of $1/B$,

$$\mathrm{i} = \frac{2\hbar k_F}{eBa} - \frac{1}{4} + \frac{\phi}{\pi}, \tag{5}$$

to find the intercept $\phi/\pi - 1/4$. An intercept value of $-1/4$ indicates a pure magnetic modulation whereas $+1/4$ suggests a pure electrostatic potential. Equation (3) captures the key features of the experimental oscillations in figure 4 and in particular the $-1/4$ phase. The experimental oscillations however decay much faster at low field than the dependence predicted by equation (3). This is partly because of momentum scattering, which reduces the probability of completing a cyclotron orbit as $\exp[-l/(2\pi R_c)]$ and because of electron–electron scattering [32]. Dampening effects aside, equation (3) can estimate $\tilde{B}_1$ from a fit of the amplitude of commensurability oscillations [28, 29].

The commensurability oscillations obtained with superconducting stripes deserve special mention here in view of the non-trivial mechanism yielding the magnetic modulation. The experiment by Carmona *et al* [26] used Pb stripes of thickness comprised between 100 and 200 nm (type II superconductor). Figures 5(a) and (b) show the distribution of magnetic flux lines when the magnetic field is ramped up and down. The modulation has troughs below the stripes and peaks between the stripes when the magnetic field is ramped up. When the magnetic field is ramped down, the difficulty in expelling pinned vortices from the superconductor causes the phase of the modulation to change by π. Flux pinning is responsible for the hysteretic behaviour of the magnetoresistance in figure 5(c). The difference between the sweep up and sweep down curves represents the magnetic commensurability oscillations. This is plotted in figure 5(d). By plotting the cut-off magnetic field of the oscillations as a function of temperature (inset), one obtains the B–T phase diagram of the superconductor. The non-hysteretic part of the commensurability oscillations in figure 5(c) originates from the build-up of strain underneath the stripes. The difference in thermal expansion coefficients of the metal and semiconductor induces a parasitic piezoelectric modulation with the same period as the magnetic modulation [27].

The commensurability oscillations are fitted in figure 6(b) to obtain the modulation amplitude that emanates from the superconducting grating. The theory accounts for the phase change of the modulation [26]. The amplitude of the magnetic modulation is plotted in panel (a) as a function of the external magnetic field. It peaks at 3 mT at the first critical field

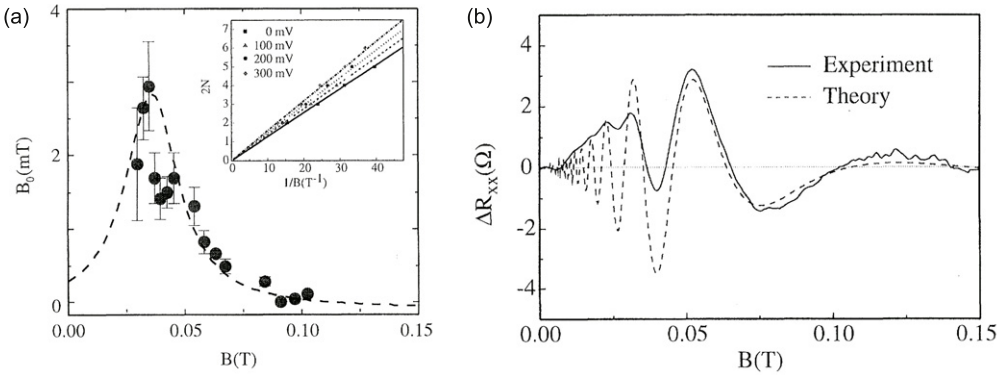

Figure 6. (a) The amplitude of the magnetic modulation applied by the Pb grating to the 2DEG. Inset: linear dependence of the maxima and minima in ΔR_{xx} on $1/B$. The slope increases $\propto n_s^{0.5}$ when a positive gate bias is applied to the 2DEG. (b) Fit of the magnetic commensurability oscillations with theory. Reproduced with permission from [26]. Copyright 1995 by the American Physical Society.

(30 mT) and vanishes at the second critical field (120 mT). The flux pinning mechanism was found to produce a magnetic modulation as long as the stripe width is large compared to the spacing between vortices. Gratings with narrower stripes (0.5 μm) were studied and revealed no magnetic hysteresis—despite the formation of clear electrostatic commensurability oscillations. It is believed that smaller superconducting elements are unable to sustain the gradient of magnetic flux that is needed to effectively modulate the 2DEG.

3.2. Giant magnetoresistance of snake orbits

Now consider magnetic modulations of large amplitude $\tilde{B}_1 > B$. The total field $B + B_{1,z}(x)$ changes sign within the superlattice period and hence subjects the 2DEG to an alternation of positive and magnetic field domains. This situation is achieved by tilting the external magnetic field with respect to the normal to the 2DEG. This decreases the normal component of the homogeneous field by $B\cos\theta$ relative to $\tilde{B}_1$. $\tilde{B}_1$ depends on the *total* magnetic field B through the magnetization which varies as $M = M(B)$—see for instance equation (1). In this way, the magnetic modulation may be saturated at an arbitrarily small value of $B\cos\theta$. In the limit of grazing tilt angles, $\theta = \pi/2$, one obtains a spatially varying magnetic field of amplitude 0.1–1.0 T with zero average.

The effect of tilting the magnetic field is shown in figure 4. A V-shaped magnetoresistance develops at low magnetic field when $B_z < \tilde{B}_1$. This magnetoresistance deserves the label of 'giant' magnetoresistance since $\Delta R_{xx}/R_0 = 1800\%$ (Co). The width and height of the magnetoresistance of the nickel sample are comparatively small, indicating a dependence on the saturation magnetization. Commensurability oscillations are seen to resume once $B_z > \tilde{B}_1$. The value of B_z at the transition from giant magnetoresistance to commensurability oscillations is therefore useful as it gives a direct reading of the modulation amplitude. As the tilt angle increases, the positive magnetoresistance region widens: $\tilde{B}_1$ increases from 30 to 140 mT (Co) and from 25 to 60 mT (Ni). What happens here is that increasing the tilt angle allows the magnetization to saturate before B_z reaches $\tilde{B}_1(M)$. At $\theta = 70°, 80°$, the magnetic modulation is already saturated by the time the transition is reached. As a result, the transition does not shift any more because $B_z = \tilde{B}_1(M_s)$. The value of $\tilde{B}_1$ at saturation can be calculated with equation (1). Using $\mu_0 M_s = 0.51$ T (Ni) and $\mu_0 M_s = 1.82$ T (Co), the calculated modulation fields are $\tilde{B}_1 = 170$ mT (Co) $\tilde{B}_1 = 75$ mT (Ni). These values are in agreement with the experimental values.

The V-shaped magnetoresistance is due to the formation of open 'snake' orbits, which we now explain. Given that the magnetic field $B_z + B_{1,z}(x)$ changes sign over one period, the 2DEG experiences alternate stripes of positive and negative magnetic field. Between two magnetic domains, the Lorentz force changes sign and redirects trajectories towards the domain boundary [33]. Electrons thus undulate back and forth in snake-like fashion as they propagate along contours of zero magnetic field—see figure 7(a). The large magnetoresistance arises from the guided motion of electrons which propagate at velocities close to the Fermi velocity. To derive the magnetoresistance of snake orbits, one first calculates the drift velocity of an orbit that crosses the line of zero magnetic field at angle ϕ:

$$v_d \simeq v_F \frac{\sin\phi}{\phi}. \tag{6}$$

There exists a angle ϕ_{max} where snake states break free from the zero field contour and bifurcate into cyclotron orbits. This is shown in figure 7(a). In the case of a *sinusoidal* modulation of amplitude $\tilde{B}_1$, ϕ_{max} is given by the condition $\cos[(\pi - \phi_{max})/2] = Ql_b$, where $Q = 2\pi/a, l_b = \sqrt{\hbar k_F/(eb)}$. $b = Q\tilde{B}_1$ is the effective magnetic field gradient at the domain boundary. For our cobalt superlattice, we find $\phi_{max} = 43°$. Cyclotron orbits at $\phi > \phi_{max}$ drift at a speed much slower than the Fermi velocity and may be considered as stationary compared to snake orbits. One therefore obtains the correction to the diffusion coefficient $\delta D_{yy} =< v_d^2 > \tau/2$ by taking the average over the bundle of snake orbits. The resistivity tensor is then obtained from Einstein's equation $\vec{\rho} = (Ne^2\vec{D})^{-1}$, where $N = 4\pi m^*/h^2$. The longitudinal resistivity is

$$\frac{\Delta\rho_{xx}}{\rho_0} = (2\phi_{max}/\pi)(\mu B_z)^2, \tag{7}$$

where μ is the mobility of the 2DEG. Figure 7(b) compares the magnetoresistance of the cobalt superlattice (dotted lines)

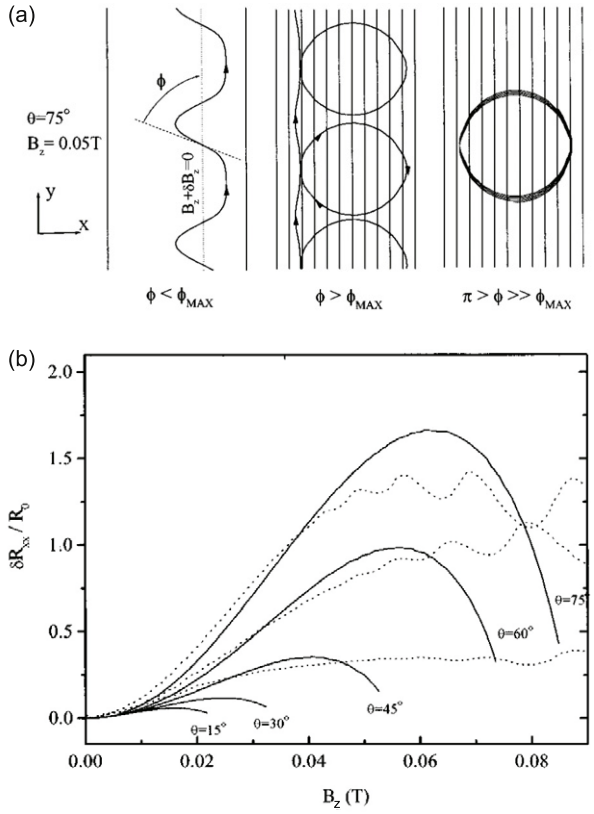

Figure 7. (a) Electron orbits calculated in the periodic magnetic field of figure 1(b). At $\phi_{\max}$, the dynamics bifurcates from snake orbits localized to one period of the superlattice (vertical interlines) to cyclotron orbits that span several periods. (b) Snake orbit magnetoresistance calculated with equation (7) (full lines) and experimental curves (dotted lines) for different angles θ. Reproduced with permission from [17]. Copyright 1997 by the American Physical Society.

to the solution of equation (7) (full lines). At low field the quadratic dependence gives a satisfactory explanation of the experiment. As B increases, the domains of negative magnetic field shrink and disappear. Snake orbits disappear ($\phi_{\max} = 0$) at $B_z = \tilde{B}_1$, leading to the collapse of the related magnetoresistance. The angular dependence of the magnetoresistance is fitted using a standard function for the magnetization curve [17]. Given that the theory contains no other adjustment parameter, the fit validates the snake orbit hypothesis.

The semiclassical nature of snake orbits is revealed by the temperature dependence of the magnetoresistance. Figure 8(a) shows that the magnetoresistance remains finite at room temperature ($\simeq$1%). The decrease in $\Delta\rho_{xx}/\rho_0$ with temperature is mainly due to the increase in background resistance ρ_0, which is activated by phonon scattering. The width of the positive magnetoresistance is also independent of temperature. This is consistent with the above interpretation since $\tilde{B}_1$ is expected to have no temperature dependence as long as the temperature remains well below the Curie temperature of the ferromagnet. The temperature dependence of the magnetoresistance amplitude is shown in figure 8(b). This exhibits a shoulder at 100 K, which represents the crossover from ballistic to diffusive transport. When $\omega_c\tau < 1$ the magnetoresistance depends inversely on D_{xx} (dotted line), whereas at $\omega_c\tau > 1$ it is proportional to D_{yy} (dashed line) [34].

3.3. Resistance resonance and Hall anomaly

Some dynamics effects are obscured in magnetic superlattices by ensemble averaging. One now seeks these effects by studying a single ferromagnetic stripe at the centre of a 2 μm wide channel—see figure 9(a). By magnetizing the stripe perpendicular to the 2DEG, one obtains a positive magnetic field domain underneath the stripe, bordered by two domains of negative magnetic field on the sides of the channel. The magnetic field profile and the amplitude of the negative magnetic step B_m are shown in the inset to figure 9(b) for Ni, Fe and Dy stripes. The domain boundary supports two types of magnetic edge states depending on the strength of the applied magnetic field B relative to B_m. When $B < B_m$, snake orbits drift along the edge. This lowers the edge resistivity (ρ_{xx}) below the Drude resistivity, ρ_0. Increasing B has the effect of depinning snake orbits and subsequently increasing ρ_{xx}. This explains the positive magnetoresistance seen at $B < B_p$ in figure 9(b). At $B = B_m$, the domains of negative magnetic field vanish and the resistivity peaks at ρ_0. When $B > B_m$, the sum of the modulation field and the applied field is positive everywhere. The magnetic boundary now supports cycloid orbits that drift along the edge of the stripe. The guided motion of cycloid orbits causes ρ_{xx} to drop sharply above the peak. This explains the resistance dip seen at $B > B_p$ in figure 9(b).

The resistance resonance effect is observed in figure 9(b) for magnetic modulations of different strengths. The peak shifts to higher field when B_m increases. However, for all samples one finds that B_p is about 50% of B_m. Figure 9(c) shows the Hall curve of the iron device normalized by the Hall curve of the unmodulated sample. Here also a resistance resonance is observed through the peak at 38 mT.

The resistance resonance and the Hall anomaly are explained within the drift–diffusion picture. Although the voltage probe separation (4 μm) is comparable to the mean free path ($l \sim 4.5$ μm), the magnetoresistance is identical with a constant factor to that measured over distances of 4, 8, 16 and 32 μm [35]. One obtains the resistivity tensor of the single stripe device as [35]

$$\rho_{xx} = \rho_0 \frac{1}{1 + 2 < v_d^2 > / v_F^2}, \tag{8}$$

$$\rho_{xy} = \frac{B}{e n_s} \frac{\rho_{xx}}{\rho_0}, \tag{9}$$

$$\rho_{yy} = \rho_0 + (\rho_0 - \rho_{xx})(\omega_c\tau)^2. \tag{10}$$

Here $\rho_0 = h/[e^2 k_F l]$ is the Drude resistivity, $k_F = \sqrt{2\pi n_s}$ is the Fermi wavevector and $v_F = \hbar k_F/m^*$ is the Fermi velocity. The magnetoresistance calculated with equation (8) is plotted in figure 10.

The anomaly in the Hall resistance is now easily explained. Equation (9) states that the ratio R_{xy}/R_{xy}^0 plotted in figure 9(c) is equal to the longitudinal resistance normalized by the Drude resistance, ρ_{xx}/ρ_0. The Hall resistance must

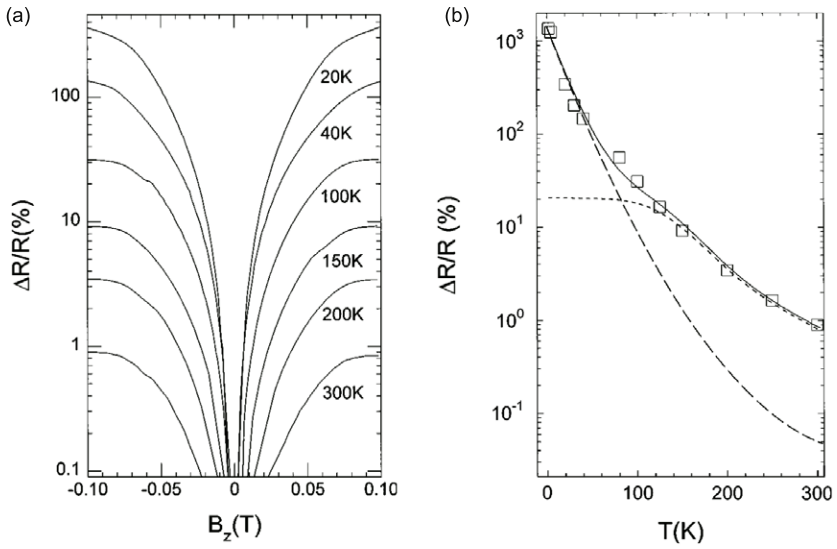

Figure 8. (a) Temperature dependence of the snake orbit magnetoresistance of a cobalt superlattice. (b) The channelling magnetoresistance (full line) has two components: a component $\propto D_{yy}$ that dominates below 100 K (dashed line) and a component $\propto D_{xx}^{-1}$ that dominates above 100 K (dotted line). Reproduced with permission from [34]. Copyright 1998, American Institute of Physics.

therefore detect the resistance resonance. The physical reason for this resides in the *inhomogeneity of the current distribution* caused by magnetic channelling. Snake orbits trap a significant fraction of the Fermi surface at the centre of the channel. These electrons lose the ability to move in two dimensions and are unable to contribute to the Hall voltage. Magnetic channelling thus decreases the Hall voltage relative to the Hall voltage of the unmodulated 2DEG when $B \neq B_{\mathrm{p}}$. When $B = B_{\mathrm{p}}$, the channelled electrons are released e.g. by the depinning of snake orbits and contribute to the Hall voltage. This gives the peak observed in figure 9(c). One concludes that when the magnetic confinement is strong enough to induce filamentary currents, the Hall resistance measures the trapping and release of electrons from magnetic edge states.

The resistance resonance effect and the Hall anomaly have been investigated in a tilted magnetic field [36]. This experiment is needed to ascertain the above interpretation, in particular to determine whether the resistance peak might not be simply due to the saturation of the magnetization. Figure 11(a) plots the ratio R_{xy}/R_{xy}^{0} as a function of B_z at tilt angles varying between 0° and 82°. The peak position stays at a *constant* value of B_z (0.12 T). When plotted as a function of the *total* magnetic field B, the peak shifts from $B = 0.12$ T ($\theta = 0°$) to $B = 2.4$ T ($\theta = 82°$). Similarly, the peak in ρ_{xx} occurs at a constant B_z rather than a constant value of B. In fact, B_{p} increases by two orders of magnitude over the range of experimental tilt angles. Recall that the magnetization depends on the total magnetic field, $M = M(B)$. If the resistance peak were an artefact of the magnetization curve such as the saturation of the magnetization, the peak would occur at constant B (not B_z). The scaling of the peak with B_z confirms the resonance condition $B\cos\theta = B_{\mathrm{m}}$ and validates the magnetic edge state picture encapsulated in equation (8). Two further remarks are necessary at this point. The variation of B_{m} with θ was neglected as it is small—see figure 1(b). Secondly, the magnetization rises sufficiently fast for snake orbits to form from vanishing magnetic fields onwards.

Magnetic channelling is further demonstrated by the temperature dependence of the magnetoresistance in figure 9(a). Dysprosium is a rare earth ferromagnet with a Curie temperature of 85 K. Above 85 K, dysprosium has a helical phase whereby spins organize in helices around the *c*-axis. In this state, the magnetization averages to *zero*. The effect of switching off the magnetization (modulation) can therefore be studied by raising the temperature through the ferromagnetic/helical phase boundary. Figure 11(c) shows that $\Delta\rho_{xx}/\rho_0$ drops from 10% at 80 K to zero at 90 and 100 K. These data show that the giant magnetoresistance arises from the magnetic potential. The importance of having magnetic potential that *changes sign* is demonstrated as follows. Quite remarkably, ferromagnetic spin alignment can be recovered by subjecting the helical phase to a magnetic field. Once the magnetic field reaches a threshold B_{H}, the magnetization jumps from zero to saturation. The modulation thus jumps to B_{m} at B_{H}. Lawton *et al* [37] have shown that the total modulation $B_{\mathrm{H}} + B_{1,z}(x)$ is always positive above 85 K. In other words, snake orbits cannot form when the magnetization jumps to saturation at $B = B_{\mathrm{H}}$. The observation of a residual peak at B_{H} in the 90 and 100 K curves, instead of a re-entrant positive magnetoresistance, demonstrates that magnetic channelling in a sign alternating magnetic modulation is the explanation for the positive magnetoresistance seen below 85 K.

Reijniers and Peeters [38] have modelled single stripe devices using the Landauer–Buttiker formula. They propose an alternative explanation to the positive magnetoresistance. As the stripe is magnetized, the number of quantum conductance channels drops, which increases the longitudinal resistance. Such a mechanism gives a peak at the saturation of the magnetization.

3.4. Magnetic dots

Magnetic potentials allow pure specular reflection of ballistic electrons. They are free from the edge roughness which causes

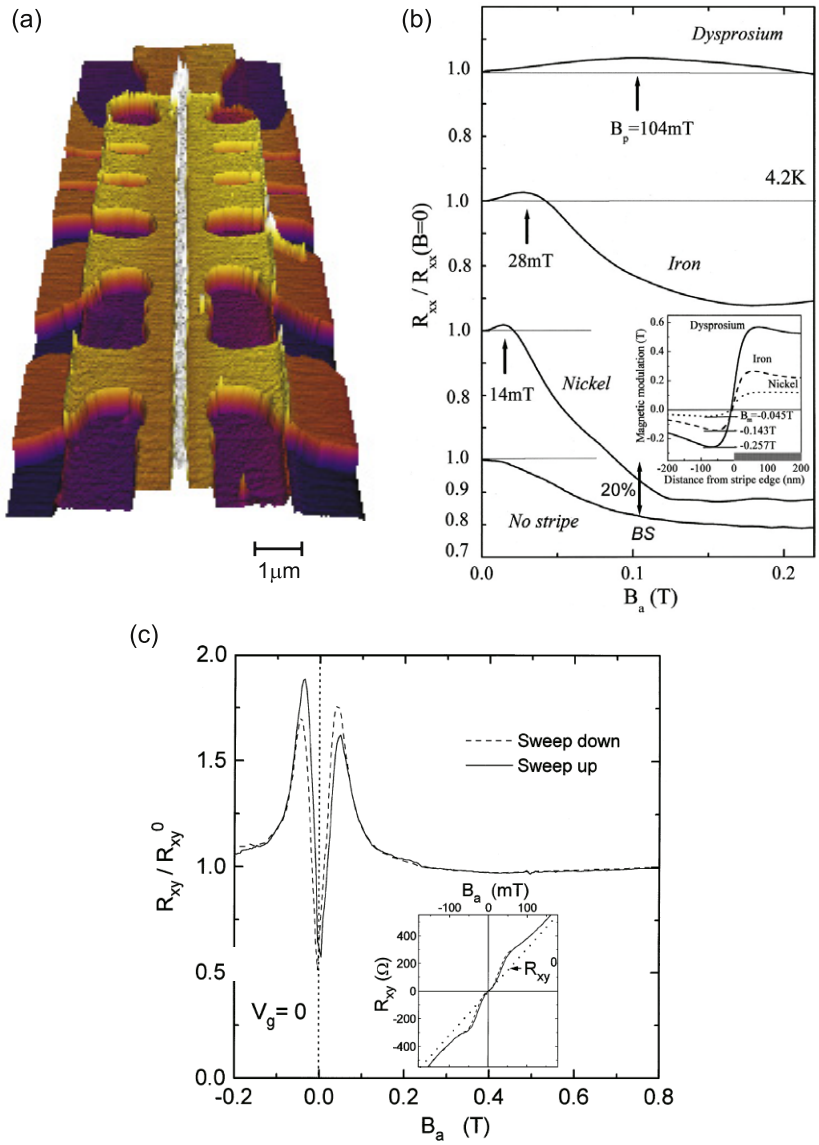

Figure 9. (a) MFM image of a single dysprosium stripe on a 2 μm wide Hall bar. (b) The longitudinal resistance of devices with nickel stripes, iron stripes, cobalt stripes and no magnetic stripe is obtained. B_a is perpendicular to the 2DEG. Inset: magnetic field profile of the Ni, Co, Dy magnetic barriers calculated with equation (36). (c) Hall curve of the iron modulated device normalized by the Hall resistance of the unmodulated 2DEG. Inset: Hall curves of modulated and unmodulated devices. Reproduced with permission from [37] and [35]. Copyright 2001 and 2000 by the American Physical Society.

diffusive scattering in electrostatic potentials. Magnetic dots are therefore well suited to studying the regular and chaotic dynamics which arises from multiple reflections on scatterers. Magnetoresistance measurements on 2D arrays of scatterers exhibit peaks that are associated with the stable orbits [39–41]. The other types of orbits are described as classically chaotic since widely different trajectories result from small differences in initial conditions. Periodic orbits are robust against the electric field applied during resistance measurements. Chaotic orbits are more easily blown away and give the low resistance states.

Uzur *et al* [42] have reported novel B-periodic oscillations in the magnetoresistance of a magnetic dot, see figure 12. Here the dynamics of ballistic electrons at the disk boundary are computed and the B-periodic oscillations are explained. The existence of a set of orbits which are stable and periodic is demonstrated. These orbits group into electronic shells made of two orbits each which bounce n times on the dot perimeter. Each shell survives up to a critical magnetic field B_n, where both orbits merge before disappearing. The depinning field B_1, $B_2, \ldots B_n, \ldots$ of consecutive shells is found to occur at regular intervals, which explains the periodicity of magnetoresistance oscillations.

Consider the circular magnetic domain of radius R shown in figure 13(a). The magnetic field is B_1 inside the disk and B_2 outside. This approximates the exact magnetic field profile shown in figure 12(a), which one obtains from equation (38). The magnetic field gradient traps magnetic edge states around the dot perimeter [43–45]. By requiring that edge states return to their point of departure after one revolution, one obtains the

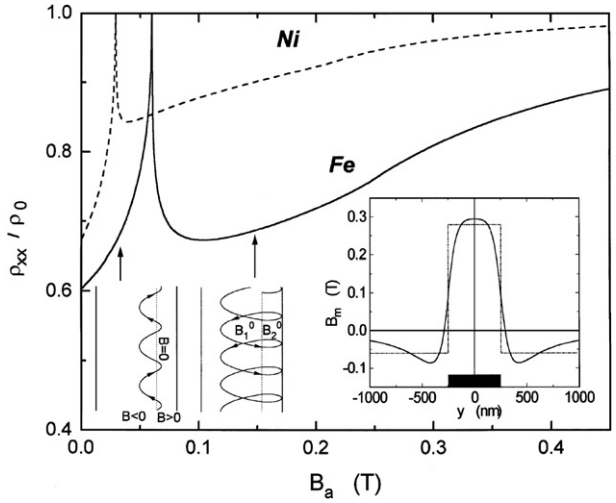

Figure 10. Theoretical magnetoresistance calculated using the drift–diffusion model, equation (8), for iron (full line) and nickel stripes (dashed line). B_a is perpendicular to the 2DEG. Inset: magnetic field profile across the 2 μm channel (full lines) and the rectangular approximation used in the model (dash–dotted lines). Reproduced with permission from [35]. Copyright 2000 by the American Physical Society.

stable periodic orbits. Starting from the equation of motion,

$$\dot{v}_x = -\omega_c(r)v_y, \tag{11}$$

$$\dot{v}_y = +\omega_c(r)v_x \tag{12}$$

one assumes that at $t = 0$ the orbit crosses the disk perimeter at O ($x = 0$, $y = 0$) with an angle φ—see figure 13(a). At a later time t_A, the orbit crosses the perimeter again at point A (x_A, y_A). By setting the condition that $(x_A - R)^2 + y_A^2 = R^2$, the integration of the equations of motion gives the excursion time t_A outside the disk. The intercept coordinates are then deduced as

$$x_A = \frac{v_F}{\omega_2}\frac{2a_2 \sin\varphi[\cos\varphi - a_2]}{[1 - a_2\cos\varphi]^2 + [a_2\sin\varphi]^2} \tag{13}$$

$$y_A = \frac{v_F}{\omega_2}\frac{2a_2 \sin^2\varphi}{[1 - a_2\cos\varphi]^2 + [a_2\sin\varphi]^2} \tag{14}$$

where $a_2 = R\omega_2/v_F$ and $\omega_2 = eB_2/m^*$. The arc of circle (O, A) defines an arc of angle θ_2 given by $\cos\theta_2 = (R - y_A)/R$. Similarly, the arc of trajectory (A, B) inside the magnetic disk corresponds to angle θ_1. One obtains θ_1 by substituting subscripts $2 \rightarrow 1$ in equations (13) and (14). In the case where B_1 and B_2 are both positive, a periodic orbit will form about the dot perimeter if the following condition is fulfilled:

$$n(\theta_2 - \theta_1) = 2\pi \qquad n = 1, 2, 3, \ldots. \tag{15}$$

Equation (15) is solved graphically in figure 13(b), where $\theta_2 - \theta_1$ is plotted as a function of φ for three values of the external magnetic field. For each value of n, equation (15) admits two solutions at the intercepts between the $\theta_2 - \theta_1$ curve and the $2\pi/n$ plateau. This indicates that there are two periodic orbits that bounce n times on the magnetic boundary and form the n shell. The periodic orbits within the $n = 4$ shell are shown in figure 14(a). Increasing B from 0.15 to 0.2 T in figure 13(b) has the effect of expelling the $n = 3$ and 4 shells from the loop. At $B = 0.25$ T, the $n = 7$ shell is about to be expelled from the dot etc. Therefore, the magnetic field corresponding to the depinning of shells $n = 1, 2, 3, \ldots$ is easily calculated as long as the parameters of the system are known. Here we use $n_s = 9 \times 10^{15}$ m^{-2}, $B_1 = B + 0.55$ T, $B_2 = B - 0.05$ T and $R = 1$ μm.

The depinning magnetic field is plotted as a function of n in figure 13(b) (full lines) at three values of the electron concentration corresponding to gate voltages of

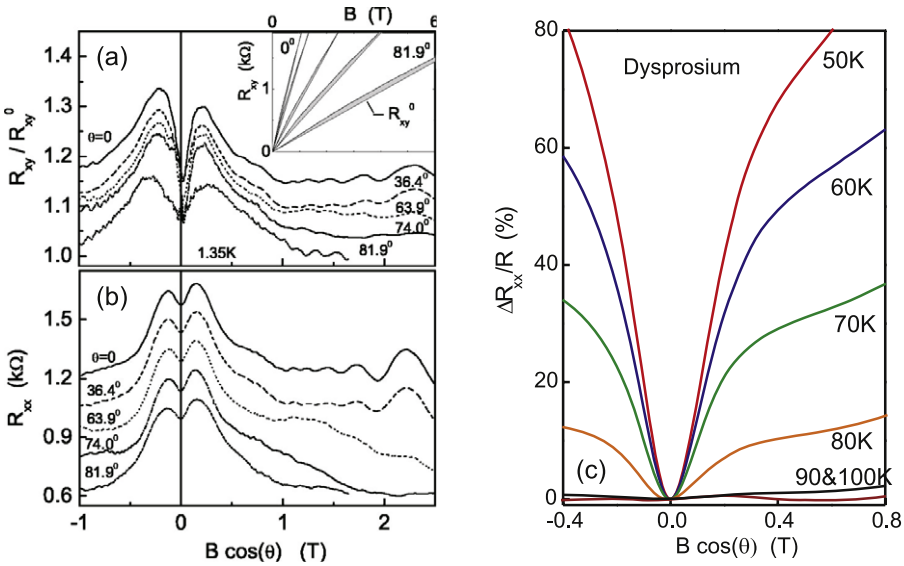

Figure 11. (a) Hall resistance of a Dy device plotted as a function of the perpendicular component of the magnetic field $B\cos\theta$ at different tilt angles, θ. The Hall curves are normalized by the Hall resistivity of the unmodulated Hall bar, R°_{xy}. Inset: Hall anomaly of magnetic waveguides (grey area) plotted as a function of B for different tilt angles. (b) Longitudinal resistance of the Dy device; (c) temperature dependence of the magnetoresistance of the dysprosium device. The magnetoresistance collapses at the Curie temperature of Dy (85 K). Reproduced with permission from [36]. Copyright 2003 by the American Physical Society.

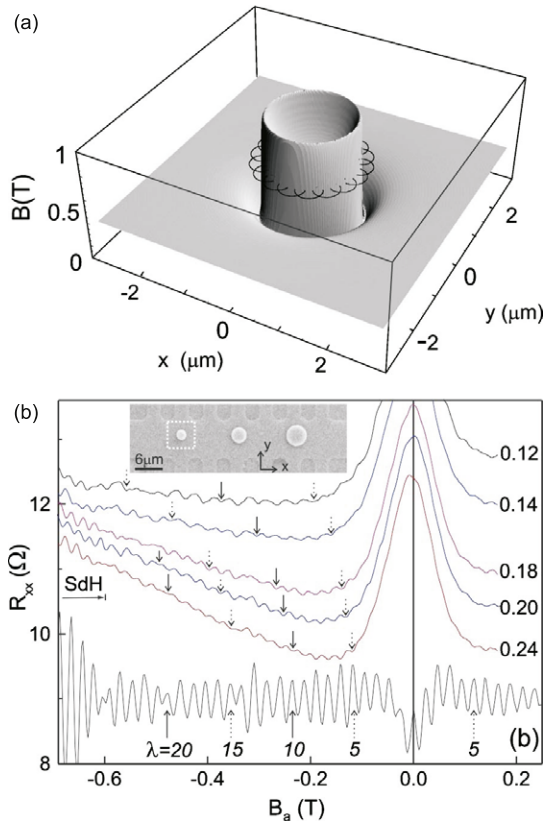

Figure 12. (a) Magnetic field generated by a 2 μm diameter dysprosium dot. The dot is magnetized perpendicular to the 2DEG by a magnetic field of amplitude 0.4 T. Magnetic edge states bounce around the circular magnetic field. (b) The magnetoresistance across the 2 μm dot shows oscillations which are quasi-periodic in B_a. Inset: Hall bar with 2, 3 and 5 μm diameter dots. Reproduced with permission from [42]. Copyright 2004 by the American Physical Society.

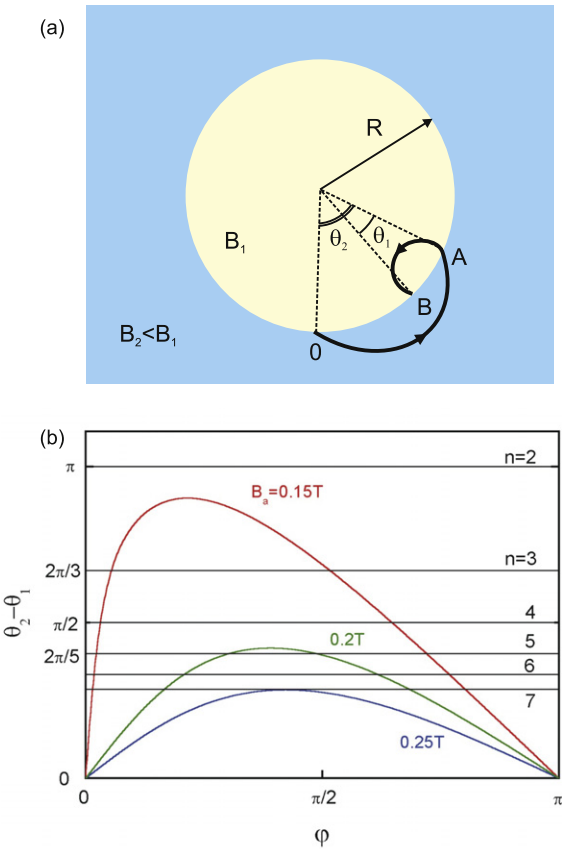

Figure 13. (a) Construction of the semiclassical orbits bouncing on the edge of a circular magnetic field; (b) graphical solution of equation (15).

0.12, 0.16 and 0.24 V (n_s increasing from 9.1 to 10.5 $\times$ 10^{15} m^{-2}). The positions of the oscillation minima in the magnetoresistance (symbols) are in excellent agreement with the theory. The theory also explains the increase in the period of oscillations with decreasing electron concentration. One therefore concludes that the semiclassical shell picture explains the B-periodic oscillations. Similar oscillations occur in 2 μm diameter *antidots*, providing confirmation that the source of oscillations is at the boundary. Quite remarkably, the amplitude of oscillations does not decrease much when the number of bounces increases. In other words, momentum information seems to be conserved after up to 25 bounces. One interprets this as evidence that reflection on magnetic interfaces is specular. This explains why these effects were not previously observed in electrostatic dots.

4. Quantum phenomena

The band structures of electrons confined by 1D magnetic potentials [5, 18, 45–50] and 2D magnetic potentials [51] has been extensively described. Since quantum phenomena have so far been reported in 1D modulations only, we will focus on magnetic fields varying in one direction. Schrödinger's equation becomes separable and can be solved as a one-dimensional problem [18]. Consider the magnetic modulation $B_{1,z}(x)$. The vector potential in the Landau gauge is $\vec{A} \equiv (0, A_y, 0)$, where $A_y(x) = \int_0^x \mathrm{d}\chi\, B_{1,z}(\chi)$. The eigenvalue equation is

$$\frac{(\vec{p} - q\vec{A})^2}{2m^*}\psi(x, y) = E\psi(x, y). \tag{16}$$

The system being invariant by translation along y, we seek solutions of the form $\psi(x, y) = \mathrm{e}^{\mathrm{i}k_y y}\varphi(x)$. Equation (16) reduces to

$$-\frac{\hbar^2}{2m^*}\frac{\partial^2\varphi(x)}{\partial x^2} + V(x, k_y)\varphi(x) = E - \frac{\hbar^2 k_y^2}{2m^*}\varphi(x), \tag{17}$$

where $V(x, k_y) = \frac{\hbar^2}{2m^*}[k_y + \frac{e}{\hbar}A_y(x)]^2$ and the $E_n(k_y) = E - \hbar^2 k_y^2/2m^*$ are the energy dispersion curves of magnetic edge states.

4.1. Magnetic quantum wires

A magnetic quantum wire forms at the boundary between positive and negative magnetic fields. Various profiles of magnetic field have been investigated for the boundary [5, 46, 52]. For simplicity, one considers the rectangular magnetic step $B_{1,z}(x) = B_m[H(x) - H(-x)]$ ($H(x)$ is the Heaviside

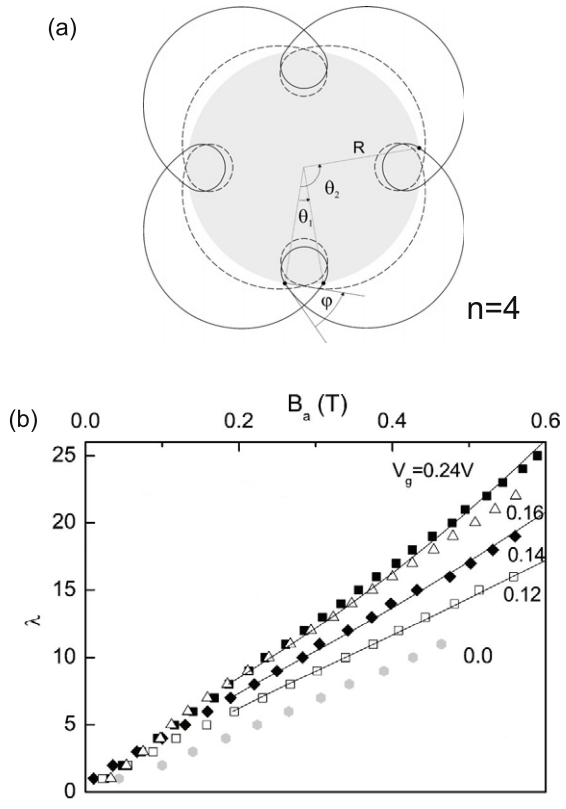

Figure 14. (a) Electronic shell ($n = 4$) consisting of two periodic orbits around the dot; (b) index of the resistance minima plotted as a function of the perpendicular magnetic field for several positive gate voltages (symbols). The full lines are the solutions of equation (15) obtained for the values of n_s corresponding to $V_g = 0.12$, 0.14 and 0.24 V. Reproduced with permission from [42]. Copyright 2004 by the American Physical Society.

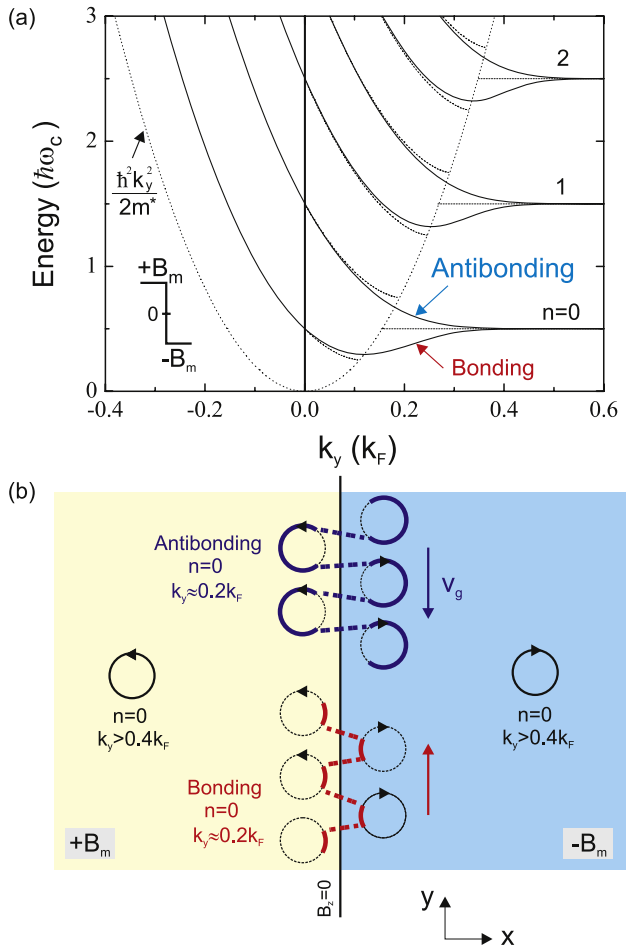

Figure 15. (a) Energy–momentum dispersion curves (full lines) in the step of magnetic field of the inset. In the classical domain bounded by the dashed line parabola, quantum states may be obtained from the WKB approximation (dotted lines). Outside the classical domain, oscillator centres couple by tunnelling through the central barrier of a magnetic double quantum well. (b) The electron trajectories in the magnetic step. The bonding edge state (red trajectory) and antibonding edge state (blue trajectory) result from the tunnelling hybridization of the clockwise rotating and anticlockwise rotating oscillators (dashed lines). The edge states propagate in opposite direction.

function) which allows discussing the essential physics without numerical complications. The vector potential is $A_y(x) = B_m|x|$ and Schrödinger's equation becomes

$$-\frac{\hbar^2}{2m^*}\frac{\partial^2\varphi(x)}{\partial x^2} + \frac{1}{2}m^*\omega_0^2\left(|x| - \frac{\hbar k_y}{eB_m}\right)^2\varphi(x) = E_n(k_y)\varphi(x). \tag{18}$$

The energy subbands $E_n(k_y)$ are calculated and plotted in figure 15(a) as a function of k_y. For each momentum k_y, there are two oscillator centres located at $\pm x_0$ where $x_0 = k_y r_m^2$ and $r_m = \sqrt{\hbar/eB_m}$ (magnetic length). The cyclotron radius in Landau level n is $R_n = \sqrt{2n+1}r_m$. The oscillators centred far from the magnetic step, $x_0 \gg R_n$, do not interact. In this case, Landau levels are doubly degenerate. The degeneracy corresponds to states rotating clockwise and anticlockwise in the regions of opposite magnetic field. When x_0 approaches the magnetic length, the oscillator wavefunctions start overlapping across the magnetic tunnel barrier. The coupling lifts the clockwise/anticlockwise degeneracy and gives the bonding and antibonding subbands shown in figure 15(a). These subbands are characterized by a positive group velocity for the bonding states and a negative one for the antibonding states. The opposite drift velocities are easily understood within the semiclassical picture of figure 15(b). At $x_0 = R_n$ ($k_y = +R_n/r_m^2$), the oscillators start to interact classically. This means that the tunnelling barrier slips below the energy of Landau level n and the system enters the semiclassical region of the energy dispersion curves within the dotted line parabola of figure 15(a). The group velocity of the bonding states reverses sign. The bonding and antibonding states then acquire the unidirectional drift characteristic of snake orbits, as seen at $k_y < 0$. In the classical regime, bonding and antibonding states retain the symmetric/antisymmetric character of their wavefunctions. Reijniers *et al* [50] have proposed to use the sign reversal of the group velocity at the minimum of the bonding subband to induce quantum interferences of snake states.

Fingerprints of the miniband structure have been demonstrated in the hybrid device of figure 16(a). This device has a magnetic stripe at the centre of the channel which is magnetized in the plane to obtain a magnetic step with

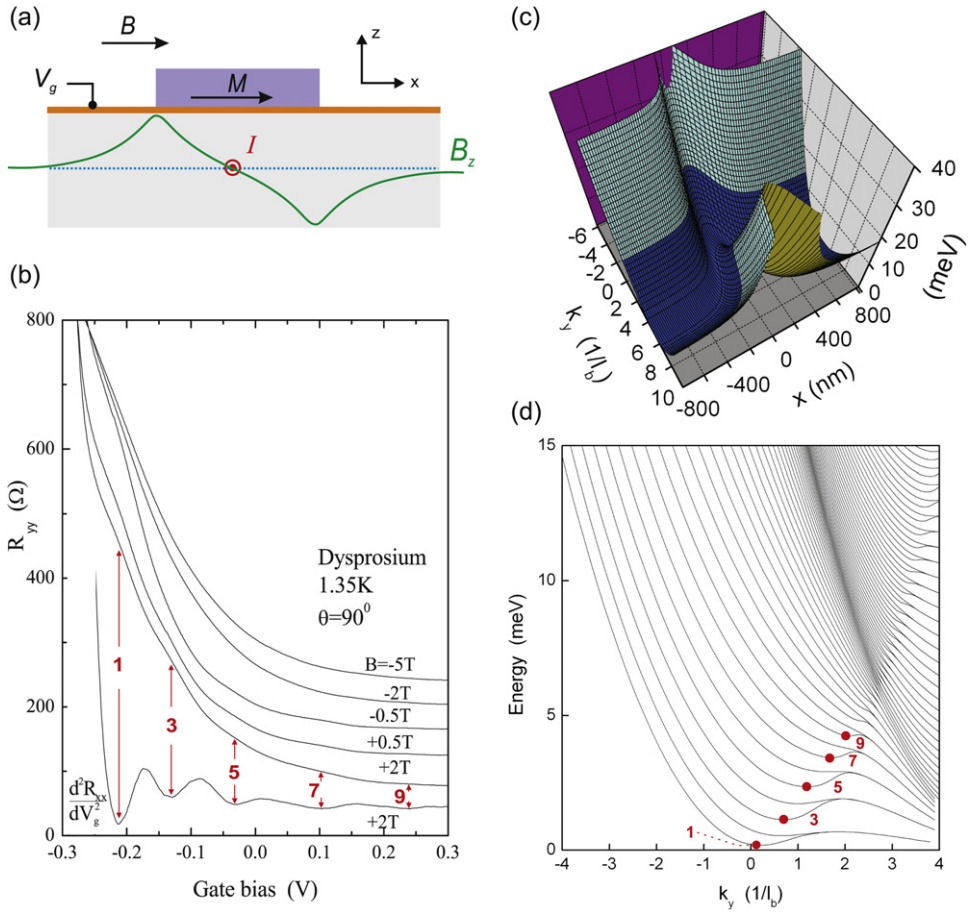

Figure 16. (a) Magnetic waveguide. (b) Dependence of the longitudinal resistance on the gate bias as the 2DEG is being depleted. (c) Magnetic potential inside the magnetic waveguide. This depends on the longitudinal wavevector and the transverse position. (d) Magnetic band structure calculated in the magnetic potential of panel (c). Parts reproduced with permission from [52]. Copyright 2009 by the Institute of Physics Publishing.

zero average. We apply a negative gate voltage, V_g, to the channel and measure the longitudinal resistance as the 2DEG is depleted. A series of resistance steps is obtained as the Fermi energy sweeps through the discrete density of states of the magnetic quantum wire—see figure 16(a). The steps are observed when the magnetization is saturated at 2 and 0.5 T but disappear during magnetization reversal at -0.5 and -2 T. The asymmetric dependence on the external magnetic field points to an effect of the magnetic modulation. To interpret the spacing between steps, we compute the electronic structure below the Fermi energy. Hall measurements at $V_g = 0$ give $n_s = 1.6 \times 10^{11}$ cm^{-2}, hence a Fermi energy of $E_F = 5.7 \pm 1$ meV. We first calculate the exact magnetic field profile at the site of the 2DEG using equation (37). Secondly, one deduces the magnetic potential $V(x, k_y)$, which we plot in figure 16(c) as a function of x and k_y. A parabolic quantum well forms at the centre of the channel where the magnetic stripe is located. This quantum well binds snake states at negative values of k_y. Thirdly, we solve Schrödinger's equation numerically to obtain the magnetic quantum subbands shown in figure 16(d). The calculation has no free parameter since all dimensions are known and the magnetization is saturated in a magnetic field of $+2$ T. One difference between the realistic band structure of figure 16(d) and the model band structure of figure 15(a) is the finite height of magnetic potential well in the former. The real magnetic field modulation decays to zero at the edges of the channel with the effect of forming doubly degenerate minibands at $k_y > 0$ in place of doubly degenerate Landau levels. Above the quantum well, virtual minibands form a quasi-continuum. Given a Fermi energy of $E_F = 5.7$ meV, magnetic subbands are filled up to subband 9—see panel (d). The Fermi level will thus cross the minima of subbands 7, 5, 3 and 1 as the 2DEG is depleted. The van Hove singularities encountered at the minima of bonding subbands are known to give dips in the conductance [46]. To estimate the change in gate bias required to move the Fermi energy from one subband to the next we use the capacitance between the gate and the 2DEG, which is $C \simeq 1.0$ mF m^{-2}. The gate voltage required to shift the Fermi energy by 1.5 meV is 64 mV. The experimental spacings between resistance steps vary between 90 and 150 mV. The agreement between theory and experiment is thus reasonable given the assumption made. One therefore interprets the five resistance steps of figure 16(a) as the sequential depletion of subbands 9, 7, 5, 3 and 1. The resistance steps are fingerprints of the quantum subbands in the magnetic quantum wire.

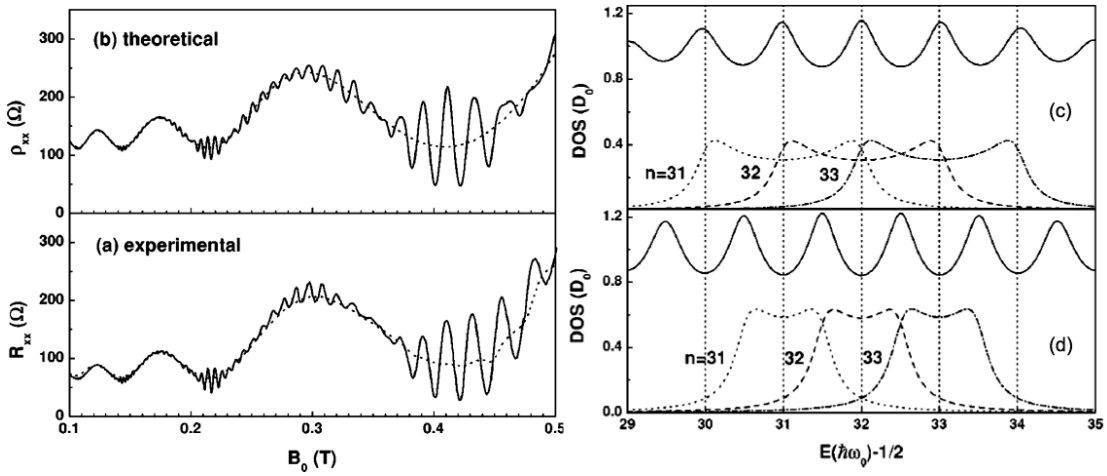

Figure 17. (a) Commensurability oscillations in the magnetoresistance of a cobalt superlattice with 500 nm period at 80 mK (full lines) and 4.2 K (dashed lines). (b) Theoretical plots. (c) Density of states of magnetic minibands $n = 31, 32, 33$. The edges of individual minibands are smeared Van Hove singularities. For the chosen ratio of cyclotron energy to miniband width, the total density of states (full lines) has maxima centred on Landau levels (vertical dotted lines). (d) Increasing the magnetic field reduces the overlap between subbands and causes the alignment of Van Hove singularities between Landau levels. The total density of states peaks between the centres of Landau levels thus shifting the phase of magneto-oscillations by π. Reproduced with permission from [54]. Copyright 2002 by the American Physical Society.

4.2. Minibands of magnetic superlattices

One now considers a periodic magnetic field with zero average and describe the general properties of its electronic structure. The effect of different magnetic field waveforms has been discussed in [46, 49]. Here one will expand on our previous example and assume a lattice of rectangular magnetic field steps $\pm B_{\rm m}$. The lattice introduces a degree of coupling between snake states which are localized near lines of zero magnetic field. There are two lines of zero magnetic field in each period. One line channels electrons along $y > 0$ and the other along $y < 0$. This symmetry needs to be conserved in momentum space, making the energy dispersion curves symmetrical about $k_y = 0$. The bonding subbands acquire two energy minima at $k_y = \pm R_n/r_{\rm m}^2$—a pure quantum mechanical effect. Now consider motion along x where the potential is periodic. Electrons can move either by tunnelling or classically depending on k_y. The classical regime is when the oscillator centres are close enough for the magnetic potential barrier between them to be less than the energy of the electron in Landau level n. This sets an upper limit on k_y, which is $|k_y| < R_n/r_{\rm m}^2$. The snake oscillators hybridize as Bloch waves. Bragg reflection at the Brillouin zone boundaries ($k_x = \pm\pi/a$) opens up energy minigaps. Away from zone boundaries, these virtual minibands have dispersion close to that of free electrons. When $|k_y| > R_n/r_{\rm m}^2$, snake states are localized in the magnetic equivalent to the Kronig–Penney potential. The weak coupling gives flat energy bands separated by wide gaps.

The internal structure of magnetic minibands has been revealed at millikelvin temperatures [53]. It should be first pointed out that commensurability oscillations are a direct consequence of oscillations of the width of magnetic minibands in the external magnetic field. Assuming a sinusoidal modulation $B_{1,z}(x) = \tilde{B}_1 \cos(Qx)$ of amplitude $B_{1,z} \ll B$, Landau levels broaden into virtual minibands centred on the Landau level energies. The energy dispersion of these minibands is given by [30]

$$E_n(k_y) \simeq (n + 1/2)\hbar\omega_{\rm c} + \hbar\omega_1 \left(\frac{ak_{\rm F}}{2\pi}\right)\left(\frac{2}{\pi Q R_{\rm c}}\right)^{\frac{1}{2}} \times \sin(QR_{\rm c} - \pi/4)\cos(Qx_0). \tag{19}$$

The width of the miniband oscillates as a function of $1/B$ and so does the group velocity $v_y = \hbar^{-1}{\rm d}E/{\rm d}k_y$. Under flat band conditions ($\sin(QR_{\rm c} - \pi/4) = 0$) the group velocity vanishes and the longitudinal resistance dips. The flat band condition is in fact identical to equation (5). Therefore, commensurability oscillations are directly implied by the miniband structure.

When the magnetoresistance is measured at 80 mK [53], fast Shubnikov–de Haas oscillations are observed about the commensurability minima—see figure 17(a). These oscillations are characterized by beats and a phase change that relates to the internal structure of minibands. In an external magnetic field of 0.1 T, the Landau gaps have a width of 2.0 K. In comparison, the miniband width oscillates between 0 and 5 K. At 80 mK, the thermal width of the Fermi surface is sufficiently small to resolve individual magnetic minibands. Edmonds *et al* [53] have shown that the fast resistance oscillation arise from the overlap of minibands. In figures 17(c) and (d), the minibands $n = 31, 32, 33$ which are nearer the Fermi level are plotted at two values of the applied magnetic field. The minibands have rounded edges, which indicate van Hove singularities smeared by collisional broadening. In panel (c), the external magnetic field causes the alignment of Van Hove singularities belonging to Landau subbands n and $n + 2$. Their superposition give peaks of the density of states at the centre of Landau levels. Increasing the magnetic field further gives the picture of panel (d) where the Van Hove singularities of Landau subbands n and $n + 1$ overlap. In this case the total density of states has maxima *in between* Landau levels. The change in overlap between subbands explains the phase reversal of Shubnikov–de Haas oscillations between peaks and troughs of commensurability

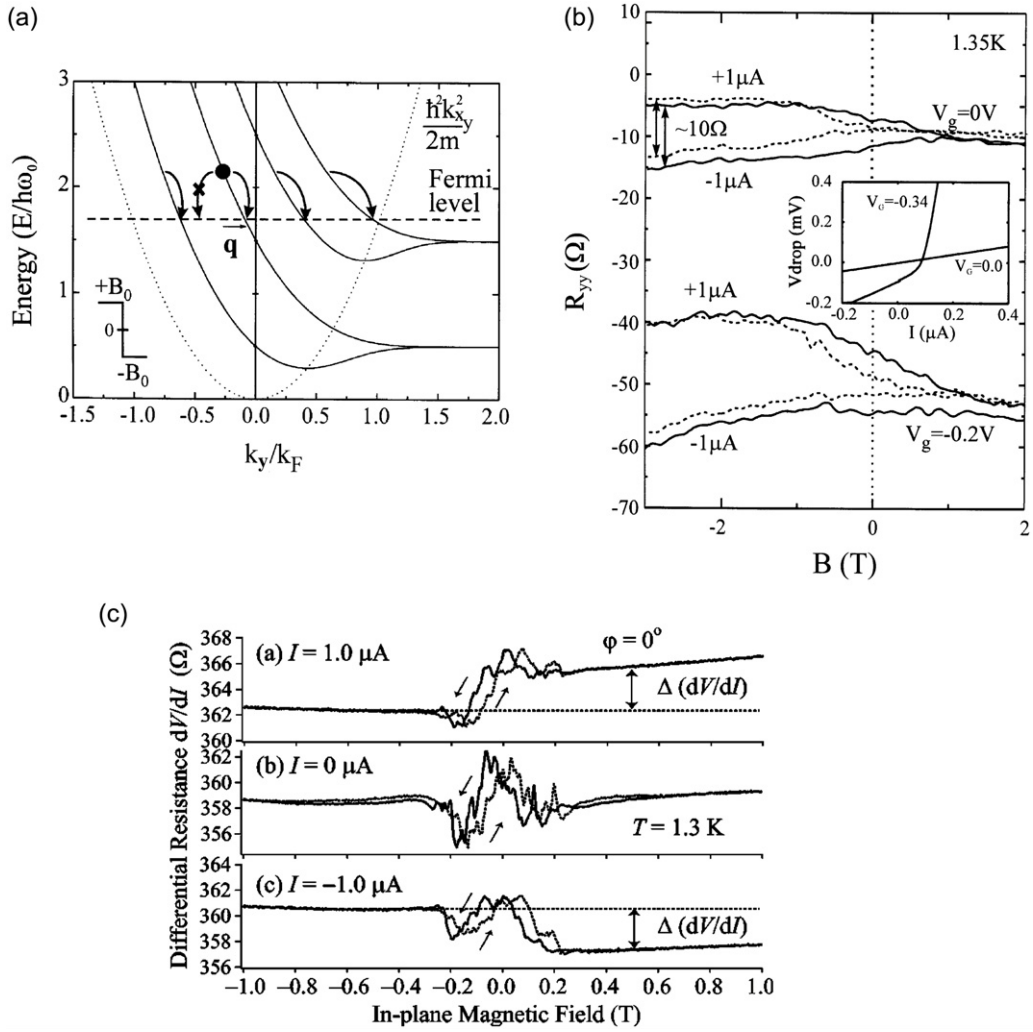

Figure 18. (a) Acoustic phonon scattering within snake orbits. (b) Non-local resistance measurements in a dysprosium magnetic waveguide. The magnetic field is swept up (full lines) and down (dashed lines). Inset: I–V curves at $V_g = 0$ and -0.2 V in an in-plane field of $+1$ T. Parameters: $d = 400$ nm, $h = 140$ nm, $z_0 = 24$ nm, $n_s = 4 \times 10^{11}$ cm^{-2}, $l = 2.2$ μm. (c) Differential magnetoresistance of a cobalt magnetic waveguide showing electrical rectification. Reproduced with permission from [55] and [56]. Copyright 2004 by the American Physical Society and 2002 by Elsevier, respectively.

oscillations. The Shubnikov–de Haas oscillations are strongest at the commensurability minima because the width of the minibands is narrowest, hence best resolved. Shi *et al* [54] have incorporated overlapping minibands into a calculation of the resistance and found excellent agreement with the experimental resistance curves as shown in panel (b).

4.3. Rectification by magnetic edge states

The peculiar asymmetry of the energy dispersion curve $E_n(k_y) \neq E_n(-k_y)$ in 15 has stimulated experiments aimed at demonstrating electrical rectification [55, 56]. These experiments were performed by applying a direct current to magnetic waveguide devices modulated by a single longitudinal stripe. The experimental set-up is the same as in figure 16. Both dysprosium [56] and cobalt [55] stripes were used at the centre of 1.5–2.0 μm wide Hall channels. The stripe was transverse magnetized by an in-plane magnetic field to define one line of zero magnetic field.

Lawton *et al* [56] first magnetized the stripe in a field of 1 T and then measured the I–V curves—see the inset to figure 18(b). They observe rectification as the channel is being depleted by a negative gate bias. The main panel shows how the rectification behaviour depends on the external magnetic field. R_{yy} is independent of the current direction at positive B; however, a splitting appears once B changes sign. The difference $R_{yy}(+1\ \mu\text{A}) - R_{yy}(-1\ \mu\text{A})$ is about 10 Ω. Furthermore, this difference increases as the 2DEG is depleted. A more refined experiment was performed by Hara *et al* [55] in the same system modulated by a field ten times weaker. The experiment was performed by superimposing a direct current $I = \pm 1$ μA on the 50 nA modulation current. This technique has the advantage of making the differential resistance at $I = 0$ accessible to the experiment. When $I = 0$, $\mathrm{d}V/\mathrm{d}I$ does not depends on the direction of B—see panel (d). Applying a finite current I introduces an asymmetry in the resistance with the direction of B: $\mathrm{d}V/\mathrm{d}I(+B) \neq \mathrm{d}V/\mathrm{d}i(-B)$. $\mathrm{d}V/\mathrm{d}I$ is high for $B > 0$ and low for $B < 0$ when $I = +1.0$ μA whereas it is

low for $B > 0$ and high for $B < 0$ when $I = -1.0\,\mu$A. $\mathrm{d}V/\mathrm{d}I$ therefore depends on the relative signs of I and $\mathrm{d}B_z/\mathrm{d}y$, the magnetic field gradient at the centre of the channel. This is because B flips the stripe magnetization, which in turn changes the sign of $\mathrm{d}B_z/\mathrm{d}y$.

Two explanations have been proposed for the observed rectification. Lawton *et al* have considered the anisotropic scattering of electrons in snake states by acoustic phonons. The asymmetric dispersion curve allows non-equilibrium electrons to thermalize by emitting a phonon of positive momentum q—see figure 18(a). The transition assisted by a phonon of momentum $-q$ is forbidden by the minigap. The anisotropic transfer of momentum to the crystal results in a phonon drag for electrons moving along the drift of snake orbits. This phonon drag is characterized by electric field F_y given by [56]

$$F_y \simeq \left(\frac{\Xi m^*}{\pi}\right)^2 \frac{r_c^3}{\rho v_l^5 e\hbar^7}(2k_B\Delta T)^5, \tag{20}$$

where Ξ is the deformation potential constant, ρ is the crystal density, v_l is the longitudinal speed of sound in the crystal and ΔT is the temperature difference between the electron and the lattice. Using $I \sim 10^{-6}$ A, $R \sim 10\ \Omega$ and $n_s \sim 10^{11}$ cm^{-2}, we obtain the power dissipated per unit area $P = I^2R/A$ and the increase in electron temperature relative to the lattice temperature $\Delta T \sim P\tau/(n_s k_B)$. The active area of the channel is $A \sim r_c L_y$, which is $\sim 10^{-8}$ cm^2 for $B_m \sim 1$ T. The acoustic phonon relaxation rate is $\tau \sim 10^{-9}$ s. These data give a temperature difference $\Delta T \sim 1$ K. Substitution of these parameters into equation (20) gives $F_y \sim 10^{-2}$ V cm^{-1}. The experimental electromotive field corresponding to the 10 Ω split in figure 18(b) is 2.5×10^{-2} V cm^{-1}.

Hara *et al* interpret I–V rectification by assuming an asymmetry in the momentum scattering rate of snake states and magnetoelectric states. The former propagate at the centre of the channel whereas the latter bounce on the edges, moving in the opposite direction to snake states. The basis for this assumption is that magnetoelectric edge states experience diffuse scattering caused by edge roughness, which is alien to snake orbits. According to this picture, the channel has low resistance when electrons diffuse along the drift direction of snake orbits and against magnetoelectric states. It has high resistance when electrons move in the opposite direction.

4.4. Quantum tunnelling through magnetic barriers

The rectangular potential barrier considered in textbook examples of quantum tunnelling is obtained here with two Dirac spikes of magnetic field $B_{1,z}(x) = B_m r_m[\delta(x + d/2) - \delta(x - d/2)]$. The double barrier potential is the potential seen by electrons arriving with normal incidence. For all other electrons, the potential barrier is $V(x, k_y) = \frac{\hbar^2}{2m^*}[k_y + r_m^{-1}(H(x + d/2) - H(x - d/2))]^2$ varies with k_y and depends on the transverse momentum. The transparency of the barrier naturally also depends on k_y. In the case of thin barriers $d < 2R_c$, the transmission switches from 0 to 1 at a critical value of k_y. These barriers behave as momentum filters. The transmission probability has been studied theoretically for various types of magnetic barriers [57, 18, 58, 44, 47].

Magnetic potentials varying on the scale of the Fermi wavelength, as required for making tunnelling barriers, are difficult to obtain using current experimental methods. The effect of reducing the barrier width down to the Fermi wavelength will now be discussed. It is useful to start by considering a homogeneous magnetic region wider than the mean free path ($d > l$) which is sandwiched by two non-magnetic regions [19]. Transport experiments that drive a current from one non-magnetic region to the other show that the magnetic region supports the entire difference of potential. The non-magnetic parts of the 2DEG, by contrast, behave as ideal contacts. Numerical simulations [59] show that a layer of charge accumulates at the boundaries between the magnetic and non-magnetic regions. The current enters at one corner of the magnetic region and exits at the opposite corner. Inside the magnetic region, the current is deflected from one edge to the other, giving rise to the Hall voltage. The resistance measured across the barrier is the two-terminal resistance since the non-magnetic regions behave as ideal contacts. This explains why it exhibits a quadratic dependence on B [19]. At higher magnetic field ($\omega_c\tau > 1$), the Hall component eventually dominates and gives a linear dependence on B.

Now consider electron transmission through magnetic barriers thinner than the electron mean free path ($d < l$). Experimentally, the magnetic field profile which gives a potential barrier closest to the square barrier is the N-shaped magnetic field profile [60–62]. This is obtained by laying a thin ferromagnetic stripe (100 nm) across the Hall channel as shown in the inset to figure 19(a). The modulation profile of the stripe magnetized in the plane is shown in figure 19(a). Figure 19(b) shows the effect of increasing the strength of the stray magnetic field B_m on the resistance of the barrier. The resistance initially increases as the magnetization tilts away from the long axis. It then saturates when the magnetization aligns perpendicular to the stripe and B_m reaches a maximum. The resistance increase accounts for the reflection of ballistic trajectories, which we now explain.

Snake orbits form for $0 < \phi < \phi_{max}$ as shown in section 3.2. These orbits are trapped at the centre of the barrier and therefore do not contribute to the resistance. The other orbits ($\phi_{max} < \phi < \pi$) are transmitted by the magnetic barrier. This is simply the momentum filtering effect of the magnetic barrier. The maximum angle is given by

$$\phi_{max} = \arccos\left(1 - \frac{e}{\hbar k_F}\int_{-\infty}^{0} B_{1,z}(x)\,\mathrm{d}x\right), \tag{21}$$

and the resistance of the magnetic barrier is [60]

$$\frac{\Delta R_{xx}}{R_0} = \frac{2\phi_{max} - \sin(2\phi_{max})}{2\pi - 2\phi_{max} + \sin(2\phi_{max})}. \tag{22}$$

Note that the magnetic barrier becomes totally opaque when ϕ_{max} approaches π.

Ballistic transmission through a thin barrier of *positive* magnetic field was studied by Vančura *et al* [63]. A similar positive magnetoresistance was observed, with the noticeable difference that it is V shaped. This was interpreted in terms

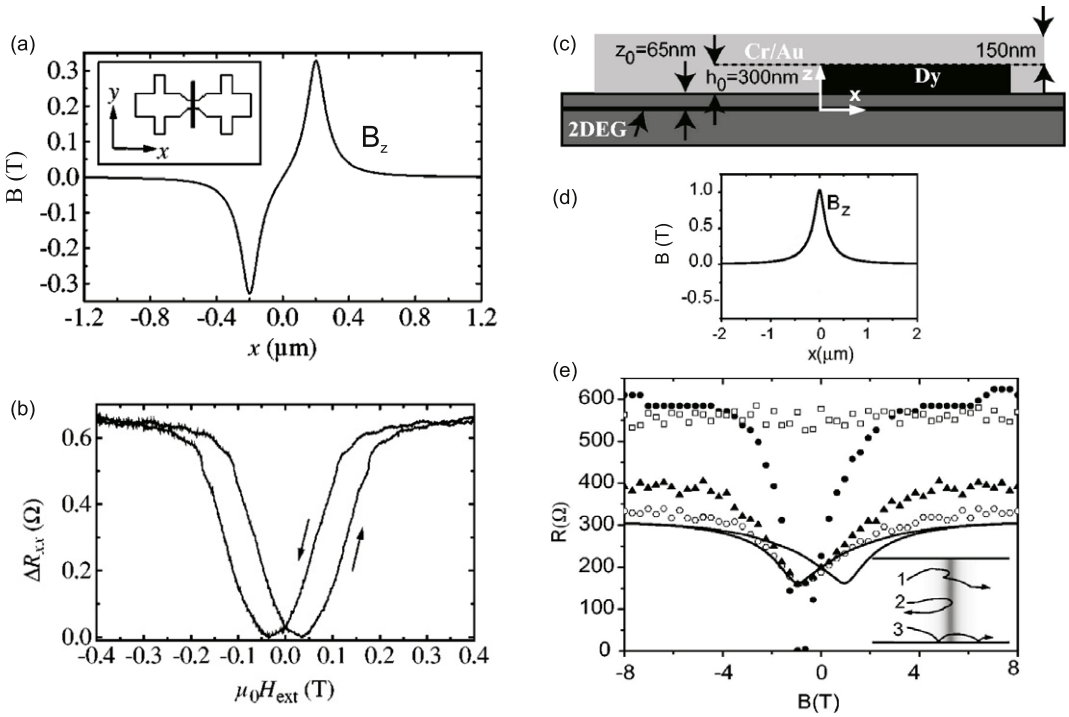

Figure 19. (a) A barrier of magnetic field is obtained by fabricating a ferromagnetic line across a 2D channel (inset). (b) Magnetoresistance of the barrier as a function of an in-plane magnetic field $\| x$. (c), (d) The fringing field at the edge of the Dy element (c) produces a localized pulse with non-zero average (d). (e) Magnetoresistance curves measured across the magnetic pulse (full lines). The symbols plot the theoretical magnetoresistance calculated in the following conditions: channel bounded by electrostatic edges and no scattering (full circles), infinitely wide channel and scattering (triangles), channel edges *and* impurity scattering (open circles). Inset: electrons can either (1) cross the magnetic pulse assisted by impurity scattering, (2) be reflected, (3) cross along the electrostatic edges. Reproduced with permission from [60] and [64]. Copyright 1999 by the American Institute of Physics and 2007 by the American Physical Society, respectively.

of the ratio of reflected to transmitted quantum conductance channels:

$$\Delta R_{xx}/R_0 = \frac{1}{N}\frac{1-\langle T\rangle}{\langle T\rangle}, \tag{23}$$

where $\langle T\rangle$ is the transmission averaged over half the Fermi surface and N is the number of modes in the channel. Equation (23) quantitatively explains the experimental magnetoresistance and predicts a positive magnetoresistance $\propto|B|$.

The above experiments have nicely established that magnetic barriers control ballistic transmission. Predicting the absolute magnitude of the magnetoresistance however requires considering sources of leakage through the barrier. One particular problem is that, in experiments, the resistance of the barrier ought to diverge at large values of $B_{\rm m}$, instead of saturating at a finite value. This problem has been investigated by Cerchez *et al* [64], who demonstrated that magnetic barriers leak through impurity scattering and magnetoelectric edge states. Their device is shown in figure 19(c). By measuring the longitudinal voltage across the edge of the dysprosium film, transport through a positive magnetic barrier could be investigated—see panel (d). The inset to panel (e) shows three electrons attempting to cross an opaque magnetic barrier. Trajectory (2) is purely ballistic and is backscattered by the magnetic field. Trajectory (1) is transmitted after scattering on one impurity. Trajectory (3) is a magnetoelectric edge state which leaks through the barrier. The effect of including both sources of leakage in calculations of the magnetoresistance is shown in figure 19(e). Including both momentum scattering and magnetoelectric edge states appears necessary to explain transmission quantitatively.

Although magnetic barriers clearly control the transmission of quantized conductance channels, there is no firm evidence that quantum tunnelling is a significant effect. One clear demonstration of magnetic tunnelling would be to observe resonant tunnelling through magnetic double barrier structures as done by Ismail *et al* [65] in lateral double barrier structures. Tunnelling transmission through magnetic potential barriers has been calculated by Matulis *et al* [18]. The difference from electrostatic barriers is that the transmission coefficient depends both on the energy and k_y as shown in figure 20(a). Figure 20(b) shows the transformation of the effective potential from double barrier at $k_y > 0$ to a double quantum well at $k_y < -d$.

4.5. Klein tunnelling in graphene

Graphene is a material of great promise for fundamental physics and applications. The absence of an energy bandgap allows switching between electron and hole conduction by gating the graphene flake. Since the conductivity never cancels, however, it is necessary to find creative new approaches to confine carriers and achieve transistor action. One such approach is to confine electrons in snake orbits by combining a homogeneous magnetic field with the action

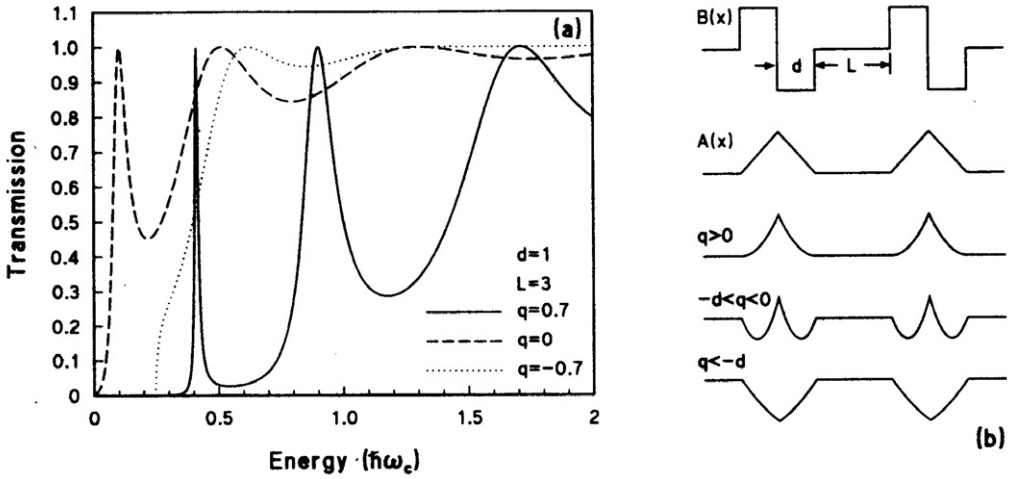

Figure 20. (a) Tunnelling transmission through a double magnetic barrier structure; (b) magnetic field profile, $B(x)$, vector potential, $A(x)$, and magnetic potential $V(x, q)$. A double barrier structure forms when momentum $q > 0$. The tunnelling spectrum exhibits well defined resonances through the quasi-bound states of the central quantum well. At $q < 0$, the magnetic barriers are replaced with quantum wells. The tunnelling probability increases to unity. Reproduced with permission from [18]. Copyright 1994 by the American Physical Society.

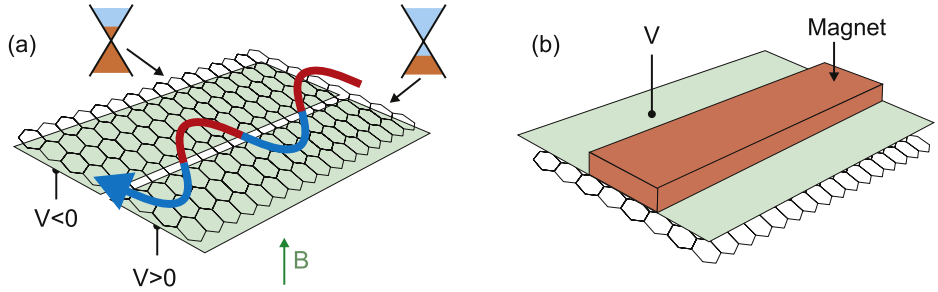

Figure 21. (a) Snake orbits in graphene. A split gate defines the interface between the electron and hole layers. The perpendicular magnetic field deflects electrons and holes towards the interface, which they cross via Klein tunnelling. Graphene thus supports extended snake orbits. (b) Magnetic gating of graphene.

of a split electrostatic gate. The graphene sheet shown in figure 21(a) has conduction by electrons in one half of the plane and conduction by holes in the other half. A magnetic field applied perpendicular to it bends electron and hole trajectories towards the interface while Klein tunnelling through the interface allows snake orbits to propagate.

Spatially varying magnetic fields offer an alternative means of tuning the electrical conduction of graphene. The magnetic modulation will for instance be obtained with micromagnets as in figure 21(b). A number of theoretical works have calculated the band structure of magnetically modulated graphene [66–68] as well as the transmission of massless electrons through magnetic barriers [69, 70]. In general, the transmission probability has the same dependence on transverse momentum as in GaAs. But the linear dispersion curve gives sharper tunnelling resonances than in systems with parabolic dispersion curves.

5. Coherent spin control with inhomogeneous magnetic fields

Here, we show how microscopic domains of positive and negative magnetic fields can be used to control the dynamics of the electron spin. We first discuss the filtering of spin currents by a gradient of magnetic field. We then describe how spin flips may be induced by shifting electrons from one magnetic domain to another. This is done either by moving electrons with electrostatic gates [71] or by using the sign reversal of the Lorentz force in snake orbits to subject the spin to an RF effective magnetic field. In the latter case, electron spin resonance is induced by a direct current [72–74]. The fluorescence of electrically induced spin resonance is discussed as it is potentially useful for making microwave sources. Finally, we observe that the Rabi frequency of the RF magnetic field is larger than the spin scattering rate in hybrid ferromagnetic/semiconductor systems. This enables coherent manipulation of the electron spin.

5.1. Spin filters

5.1.1. Mesoscopic Stern–Gerlach effect. The experiment by Wróbel *et al* [75] demonstrates the Stern–Gerlach effect in a mesoscopic hybrid device. Two magnets are fabricated on each side of a GaAs/AlGaAs channel to apply a spatially varying magnetic field to the central region—see figure 22(a). When the two magnetizations are antiparallel, the in-plane magnetic

field component varies linearly across the channel and changes sign at the centre. The poles that face each other across the channel are the same, hence the magnetic field emanates from them in opposite directions. When the two magnetizations are parallel, the in-plane magnetic field in the central region is constant. To ensure that the antiparallel configuration occurs over a significant range of magnetic field, Wróbel *et al* used one hard (Co) and one soft (Py) magnet—see figure 22(b). They take the additional precaution of levelling the centre of the magnetic film with the height of the 2DEG to cancel the perpendicular component of the stray magnetic field at the site of the 2DEG. Finally, the Permalloy layer is made thicker than the cobalt layer to compensate for the higher magnetization of cobalt and obtain a modulation with zero average field (antiparallel magnetizations).

The gradient of magnetic field is $b_y \approx 10^6$ T m^{-1} when the magnetizations are antiparallel. Otherwise, the magnetic field is homogeneous and equal to $B_y = 0.3$ T when the magnetizations are parallel. Outside the shaded region of the Hall curves in figure 22(c), $B_y = 0.3$ and $\langle B_z \rangle = 0$, which gives $R_{xy} = 0$. In the shaded region, the magnetic field gradient exerts a Zeeman force on the ballistic current, $F_y = \pm g\mu_B b_y/2$, where g in the Landé factor. The current component deflected to the left (I_1) and the one deflected the right (I_2) are shown in figure 22(d) as a function of B. I_1 and I_2 are clearly enhanced in the field range where the magnetizations are antiparallel. This suggests that spin currents are split by the Zeeman force. The asymmetric magnetic field dependence seen in I_1 and I_2 is due to a residual Hall component. This is eliminated by plotting $I_s = (I_1 + I_2)/2$—see the inset to figure 22(d). The peak in I_s demonstrates the splitting of the incoming current into two spin polarized components.

5.1.2. Spin filtering by magnetic rings. The dephasing of the spin wavefunction by a spatially inhomogeneous magnetic field controls the conductance of mesoscopic ring structures. An electron moving in a textured magnetic field accumulates a geometric phase along the ring perimeter. The transmission is maximum when the phase acquired around the ring is an integer multiple of 2π. One example of textured magnetic field is the effective magnetic field produced by spin–orbit interaction. This field is perpendicular to the electron momentum, hence, in a ring geometry, the effective magnetic field has circular symmetry. Spin interferences occur as the electron spin precesses around clockwise and anitclockwise rotating magnetic fields in both arms of the loop. A perpendicular electric field tunes the precession frequency by controlling the strength of spin–orbit interaction. Conductance oscillations due to interferences of the spin wavefunction have been reported by Nitta *et al* [76] when a gate bias is used to tune the strength of the spin–orbit interaction.

A similar effect is obtained in mesoscopic hybrid devices where ring shaped ferromagnets are used to produce a field with circular symmetry. The transmission of electrons through such rings has been investigated theoretically by Frustaglia *et al* [77–79]. Figure 23(a) shows the transmission through a loop subjected to a circular magnetic field and a magnetic flux

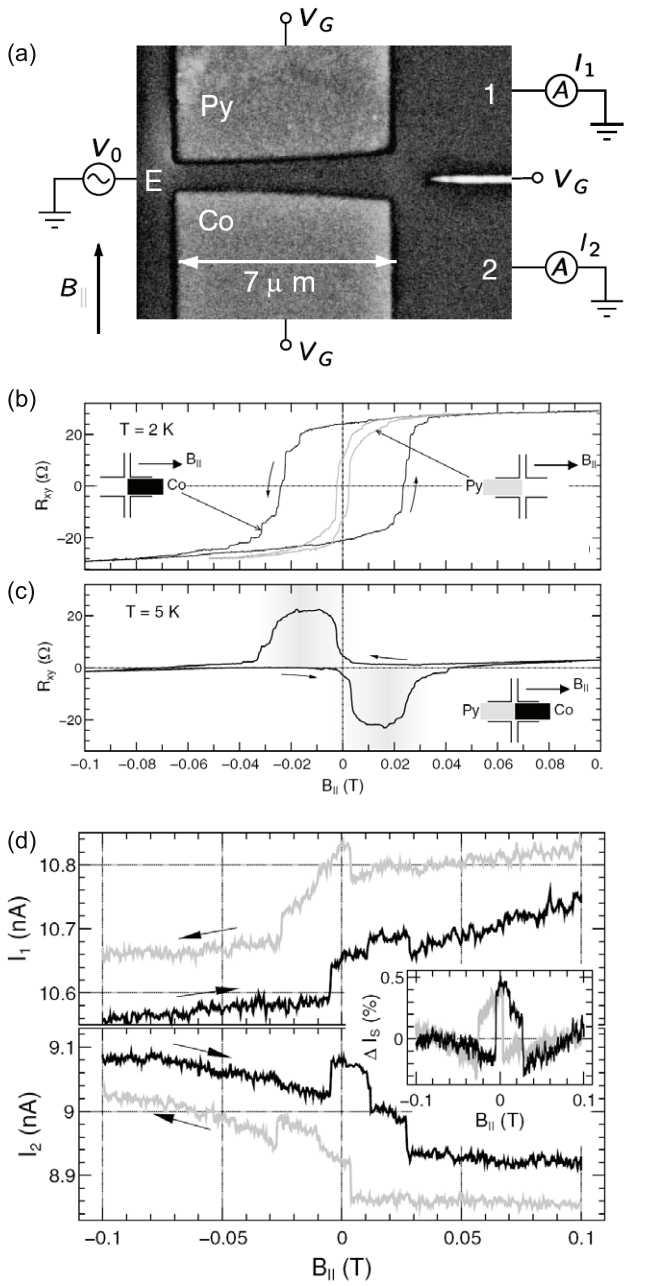

Figure 22. (a) Spin filtering using the Stern–Gerlach effect. Permalloy and cobalt gates are magnetized by $B_\parallel$. (b) The individual magnetization curves of the Co and Py gates. (c) Magnetization curve of the combined Co and Py gates showing compensation when the magnetizations are aligned. (d) The currents, I_1 and I_2, deflected by the magnetic gradient. Inset: the deflected current $I_s = (I_1 + I_2)$ symmetrized to eliminate the residual Hall voltage. I_s is maximum when the Py and Co gates have antiparallel magnetization and apply a magnetic field gradient. Reproduced with permission from [75]. Copyright 2004 by the American Physical Society.

ϕ through the loop. As the strength of the circular magnetic field increases from panel (b) to (d), this field tunes the transmission of spin up and spin down currents. Remarkably, the total transmission (spin up + spin down) is also strongly modulated by the strength of the circular magnetic field, especially when the magnetic field through the ring is $\phi_0/2$ and $\phi_0(\phi_0 = h/2)$.

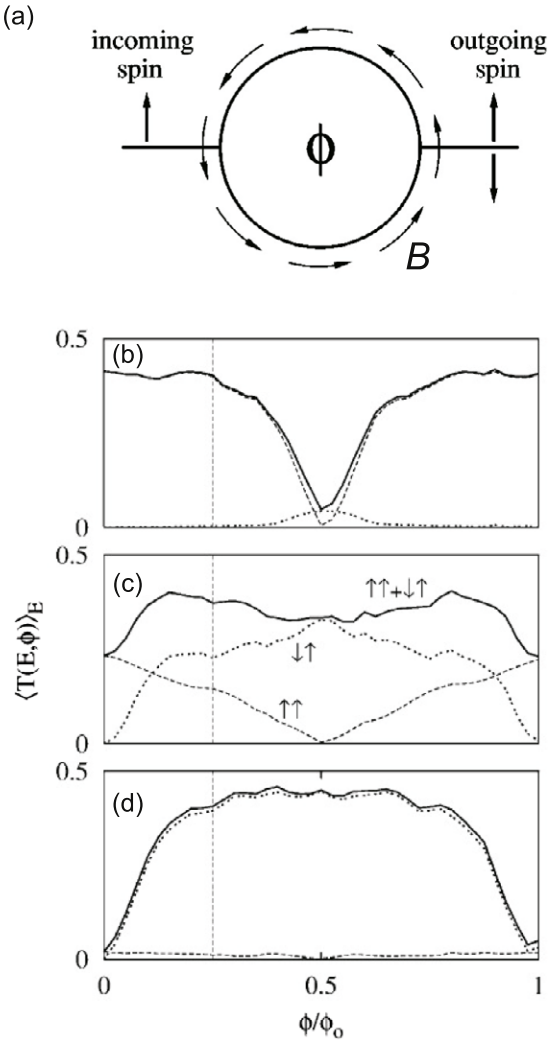

Figure 23. (a) Ring geometry with a circular magnetic field; (b)–(d) transmission of spin currents as a function of the magnetic flux. As the strength of the circular magnetic field increases—from top to bottom—the transmission via spin flips increases. Reproduced with permission from [77]. Copyright 2001 by the American Physical Society.

5.2. Electrically induced ESR

We now consider the dynamics of the electron spin in snake orbits. In the device of figure 24(a), the stray magnetic field threads the 2DEG with an in-plane component B_0 which is roughly constant and an out-of-plane component $B_1(y)$ which changes sign at the centre of the channel. The perpendicular component has an approximately linearly dependence characterized by gradient $b \equiv \mathrm{d}B_1/\mathrm{d}y = 2T/\mu\mathrm{m}$. Snake orbits form at the centre of the channel. In addition to the perpendicular field, the electron *spin* experiences an in-plane magnetic field $B_0 + B$ which includes the contribution of the external magnetic field used to magnetize the ferromagnetic stripe. This is a large magnetic field which defines the frequency of spin precession ω_0. The meandering of snake orbits between domains of positive and negative magnetic field subjects the spin to a time dependent effective magnetic field $B_1(t)$, which oscillates at the frequency of the snake orbit, ω_1. The crossed dc and ac magnetic fields induce electron spin resonance when $\omega_1 = \omega_0$.

The frequency of snake orbits is obtained by solving the semiclassical equation of motion corresponding to electrons on the Fermi surface [72, 73]. The frequency of transverse oscillations is parametrized by θ, the angle at which the snake orbit crosses the line of zero magnetic field ($\theta = \pi - \phi$ of section 2.2). One finds that the transverse equation of motion is the equation of an *anharmonic* oscillator of fundamental frequency $\omega_1 = \pi/[2\tau_b F(\pi/2, \theta)]$, where

$$F(\chi, \theta) = \int_0^{\chi} \frac{\mathrm{d}\alpha}{\sqrt{1 - \cos^2(\theta/2)\sin^2(\alpha)}}, \qquad (24)$$

$\chi = \arcsin\sqrt{Z^2/[\cos^2(\theta/2)(Z^2 + \sin^2(\theta/2)]}$ and $\tau_b = m^*/\sqrt{\hbar k_F e b}$. The dispersion curve of oscillator modes is plotted in figure 24(b). The dispersion has a cut-off frequency at $\omega_c = 1/\tau_b$. In a GaAs quantum well with $n_s = 1.6 \times 10^{15}\ \mathrm{m}^{-2}$ and $b = 2\ \mathrm{T}\ \mu\mathrm{m}^{-1}$, one has $\omega_c/2\pi = 150$ GHz. The snake orbit trajectories and the Fourier harmonics of transverse oscillations are plotted in figures 24(c)–(h) for three values of θ. $\theta = 0^+$ is the angle of slow oscillators at the centre of the dispersion curve. At $\theta = 40^0$, the drift of snake orbit changes sign. $\theta = \pi$ corresponds to snake orbits oscillating at the cut-off frequency ω_c. The amplitude of transverse snake oscillations is $Z = \cos(\theta/2)$.

Satellites of the main ESR line arise for two reasons. Firstly, the anharmonicity of the snake oscillator gives additional resonances when the Larmor frequency matches the high harmonic frequencies of the oscillator. In this case, absorption peaks occur when $\omega_0 = \omega_1/(2k + 1)$ where $k = 0, 1, 2, \ldots$. A second series of satellite peaks arises due to the non-linearities of magneto-dipole interaction which allow multiple photon absorption processes. The time dependent magnetic field $B_{1,z}(t)$ is linearly polarized along z and may be viewed as the sum of two circularly polarized waves rotating clockwise and anticlockwise. The non-linearity of the Bloch equations gives additional terms in the susceptibility which are proportional to $\tilde{B}_1^2$, $\tilde{B}_1^4 \ldots$. These terms mix clockwise and anticlockwise polarizations. Their amplitude is large and comparable to the leading term in the series expansion of the susceptibility. The reason for this is that the oscillating field $\tilde{B}_1$ in snake orbits ($\approx$1 T) is huge, 10^5–10^6 times larger than the magnetic field component of microwave generators ($\approx$1 mW cm^{-2}). In this case, the rate of spin flips assisted by a cascade of $n = 3, 5, \ldots$ circularly polarized photons becomes significant compared to spin flips assisted by the absorption of a single photon. The photons involved in the cascade have energy $\hbar\omega_0/n$. The angular momentum of the photons in the cascade adds up to $\pm\hbar$, which is the angular momentum gained or lost during spin flip. The optical non-linearities of the magneto-dipole susceptibility have been calculated in [80]. Multiple photon processes give a second series of absorption peaks at Larmor frequencies given by $\omega_0 = (2k + 1)\omega_1$.

5.3. Spin resonance fluorescence

An important consequence of the large RF magnetic field $B_1(t)$ is that, at resonance, spins flip at very high frequency. The

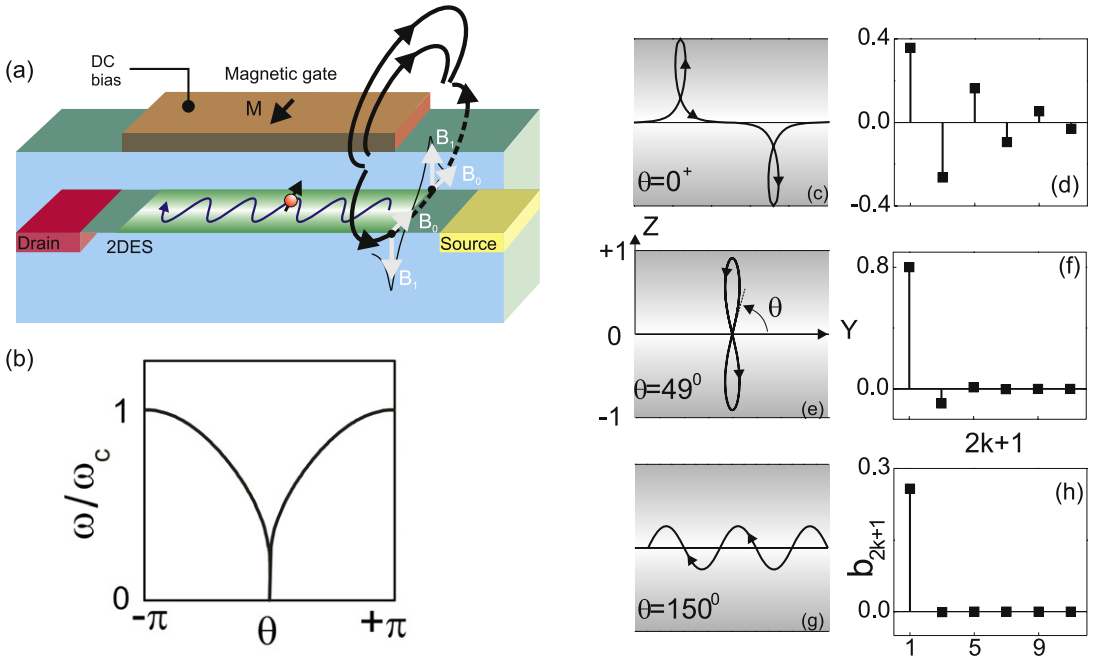

Figure 24. (a) Spin resonance fluorescence device; (b) frequency dispersion curve of snake orbit oscillators as a function of the angle at which the snake orbit crosses a line of zero magnetic field; (c)–(h) semiclassical snake orbits and the Fourier spectrum of their transverse oscillations. Reproduced with permission from [73]. Copyright 2001 by the American Physical Society.

flip rate is determined by the Rabi frequency $\tilde{\Omega}_1 = g\mu_B \tilde{B}_1/\hbar$, which is of the order of the GHz. The Rabi frequency is comparable to the momentum relaxation rate in the 2DEG and is much faster than the magneto-dipole radiation rate:

$$\Gamma = \frac{1}{3}\frac{(g\mu_B)^2 k^3}{ce^2}\alpha. \tag{25}$$

Under these conditions, electrically induced spin resonance can emit a strong microwave fluorescence through a radiative cascade mechanism which we now describe. The process is depicted in the three level diagram of figure 25(a). The spin flip transition propelled by spin oscillators occurs between states $|a, 0\rangle$ and $|b, 0\rangle$ at rate Ω_1. The photon number is constant because spin flips are driven by the d.c. bias. In the excited state, the spin may decay into state $|1, \mathbf{k}p\rangle$ by spontaneously emitting a photon with random momentum $\mathbf{k}$ and polarization p. The rate of spontaneous decay Γ being small compared to Ω_1, several cycles of Rabi oscillations take place before one spontaneous emission event. After this has occured, Rabi oscillations resume until a second photon is spontaneously emitted and so on. The opening of parallel pathways for spontaneous emission initiates a radiative cascade which sustains microwave emission as snake orbits move along the magnetic waveguide of figure 24. The cascade phenomenon is closely related to photon antibunching in optics. A current injected with no spin polarization gives the fluorescence power calculated in [73, 74] and plotted in figure 25(b). Each curve represents the cumulated microwave power emitted until time t for different values of the ratio $r \equiv \tilde{\Omega}_1/\Gamma$. When $r < 1$, spins prepared in the excited state decay into the ground state. There is no way back into the excited state since the Rabi frequency is too slow. As a result, the emitted power drops to zero on the timescale of spontaneous emission. When $r > 1$, the Rabi oscillations sustain the radiative cascade and the cumulated microwave power increases superlinearly with time.

Panel (c) maps the fluorescence power emitted by individual snake orbits θ when the frequency of Larmor precession ω_0 increases from 0 to $3\omega_c$. The emission spectrum shows the weaker contribution of harmonics $k = 1, 2, \ldots$ relative to the fundamental frequency $k = 0$. The fluorescence power increases with the oscillator frequency because the magneto-dipole coupling increases as $\propto\omega^3$ after equation (25). The emitted power is therefore maximum for the fastest snake orbits at frequency ω_c. The spin resonance condition specifies that $\omega_0 = \omega_c$. This explains why the peak is seen at $\omega_0/\omega_c \sim 1$. Since $\omega_c \propto n_s^{1/4}$, the peak emission frequency may be tuned with an electrostatic gate. This effect promises tunable microwave emitters with emission frequency in the range 0–500 GHz and output power in the range of 100 nW μm^{-2} [73, 74].

5.4. Coherent population trapping

The trapping of snake states in magnetically modulated 2DEGs makes the *coherent manipulation of the electron spin* accessible to the experiment. Electrons in snake orbits experience a RF magnetic field of amplitude considerably larger than that obtained from electromagnetic waves. This makes the Rabi frequency of electrically induced spin resonance of same order of magnitude as the momentum scattering rate in the 2DEG. Any perturbation to the coherent dynamics of the electron spin will therefore have directly measurable effects on propagation of snake orbits. Blocking

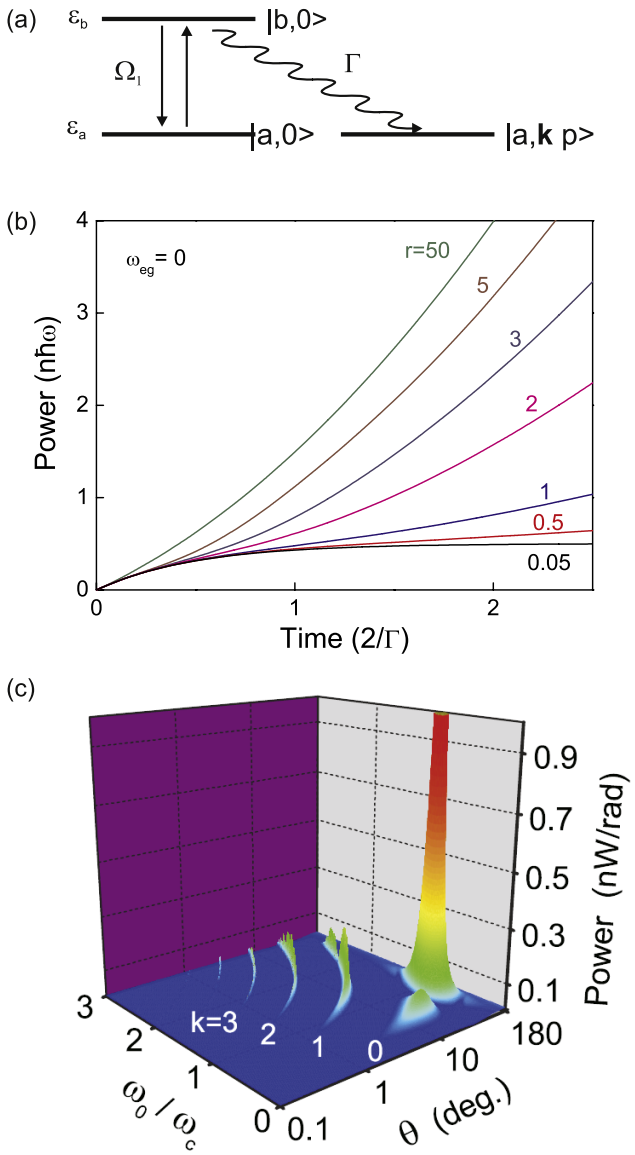

Figure 25. (a) Energy diagram of electron spin resonance fluorescence. Rabi oscillations (Ω_1) compete with spontaneous recombination (Γ). (b) Amplification of microwave emission through the radiative cascade. $\Omega > \Gamma$ ($r > 1$) initiates the radiative cascade. (c) Microwave power emitted by individual snake orbits (θ) as a function of the in-plane magnetic field (ω_0). Reproduced with permission from [73]. Copyright 2001 by the American Physical Society.

spin flips has the effect of inhibiting the propagation of snake orbits at low temperature. This is the effect that is achieved in the coherent population trapping experiment described below.

A schematic diagram of the experimental set-up is depicted in figure 26(a). A cobalt superlattice is magnetized in the plane to obtain a magnetic modulation with zero average. Snake states form within each period of the superlattice. A grating rather than a single stripe is used to amplify changes in resistance due to magnetic channelling. Electron spin resonance occurs within snake orbits when the frequency of transverse oscillations ω_1 equals the Larmor frequency ω_0. One then irradiates the surface of the sample with unpolarized microwaves at frequency ω_r. This introduces a spin flip channel that competes with the spin oscillator driven transition. The energy diagram of both transitions is shown in figure 26(b). The snake oscillator transition links $|\downarrow, N\rangle$ and $|\uparrow, N\rangle$. It leaves the number of photons present in the cavity unchanged. This transition is always resonant because the spectrum of snake orbits between 0 and ω_c is continuous—see figure 24(b). One oscillator mode is always resonant since the resonant condition $\omega_1 = \omega_0$ is always satisfied. This transition strongly couples levels $|\uparrow, N\rangle$ and $|\downarrow, N\rangle$ with Rabi frequency Ω_1. By contrast, the microwave induced transition couples states $|\uparrow, N+1\rangle$ and $|\downarrow, N\rangle$. The detuning from resonance is $\Delta = \omega_0 - \omega_r$. The microwave transition gives a much weaker coupling than the snake oscillator transition $\Omega_r \ll \Omega_1$.

When the microwave transition crosses resonance, the initial states couple through the final state and hybridize to form a dark state: $|d\rangle = \frac{\Omega_1}{\sqrt{\Omega_1^2+\Omega_r^2}}|\uparrow, N+1\rangle - \frac{\Omega_r}{\sqrt{\Omega_1^2+\Omega_r^2}}|\uparrow, N\rangle$ [81]. The spin system evolves towards the dark state with no way out since the dark state has no amplitude of probability on $|\downarrow, N\rangle$. The probability of the dark state is given by the expectation of the density matrix of the system $\hat{\rho}$ in the dark state:

$$P_{\text{dark}} = \langle d|\hat{\rho}|d\rangle. \tag{26}$$

To calculate the density matrix one considers the Hamiltonian of the system $\hat{H}_0 = \hbar\omega_0|\downarrow, N\rangle\langle\downarrow, N|$. The interaction Hamiltonian of the three level system coupled by the two transitions is

$$H_{\text{int}} = -\frac{\hbar}{2}\begin{pmatrix} 0 & 0 & \Omega_r \\ 0 & 2\Delta & \Omega_1 \\ \Omega_r & \Omega_1 & -2\Delta \end{pmatrix}. \tag{27}$$

The density matrix evolves according to the following rate equations [81] where γ_T and γ_L are the transverse and longitudinal spin relaxation rates:

$$\dot{\rho}_{11} = \frac{i}{2}\Omega_r(\rho_{31} - \rho_{13}) + \rho_{33}\frac{\gamma_T}{2} \tag{28}$$

$$\dot{\rho}_{22} = \frac{i}{2}\Omega_1(\rho_{32} - \rho_{23}) + \rho_{33}\frac{\gamma_L}{2} \tag{29}$$

$$\dot{\rho}_{33} = \frac{i}{2}[\Omega_r(\rho_{13} - \rho_{31}) + \Omega_1(\rho_{23} - \rho_{32})] - \rho_{33}\gamma_L \tag{30}$$

$$\dot{\rho}_{12} = \frac{i}{2}[\Omega_r\rho_{32} - \Omega_1\rho_{13}] + \frac{1}{2}\rho_{12}(2i\Delta - \gamma_T) \tag{31}$$

$$\dot{\rho}_{13} = \frac{i}{2}[\Omega_r(\rho_{33} - \rho_{11}) - \Omega_1\rho_{12}] + \frac{1}{2}\rho_{13}(2i\Delta - \gamma_L) \tag{32}$$

$$\dot{\rho}_{23} = \frac{i}{2}[\Omega_1(\rho_{33} - \rho_{22}) - \Omega_r\rho_{21}] + \frac{1}{2}\rho_{23}(0 - \gamma_L). \tag{33}$$

One seeks the time independent solutions by successive approximations to second order in Ω_r/Ω_1. Taking $\rho_{11} \approx 1$, $\rho_{22} \approx 0$, $\rho_{33} \approx 0$ as initial conditions and assuming that $\gamma_L \cong \gamma_T$ for conduction electrons, one obtains

$$P_{\text{dark}} = \frac{4\Omega_1^2\Omega_r^2}{\Omega_1^2+\Omega_r^2}\frac{\Omega_1^2 + \gamma_L\gamma_T}{(\Omega_1^2 + \gamma_L\gamma_T - 4\Delta^2)^2 + 4\Delta^2(\gamma_L+\gamma_T)^2}. \tag{34}$$

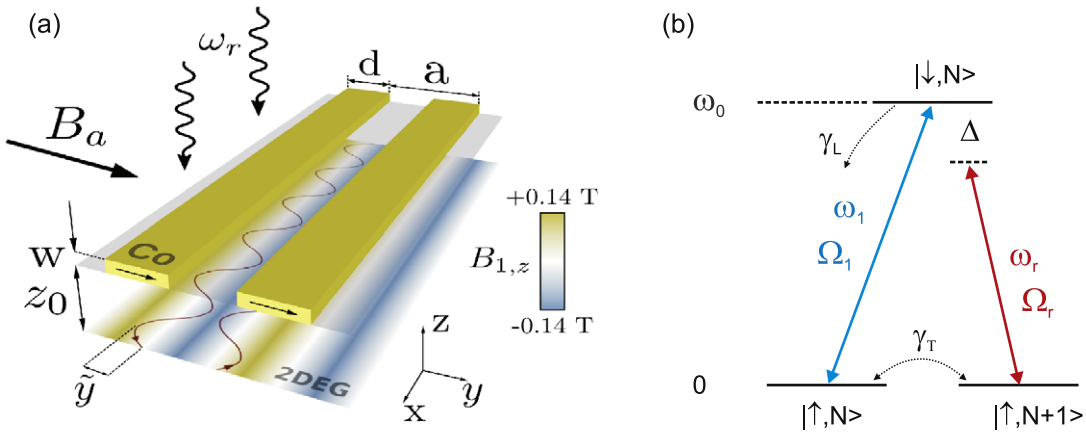

Figure 26. (a) Magnetic superlattice irradiated with microwaves; (b) the microwave transition (ω_r, Ω_r) and the spin oscillator transition (ω_1, Ω_1) couple states with the same spin at resonance.

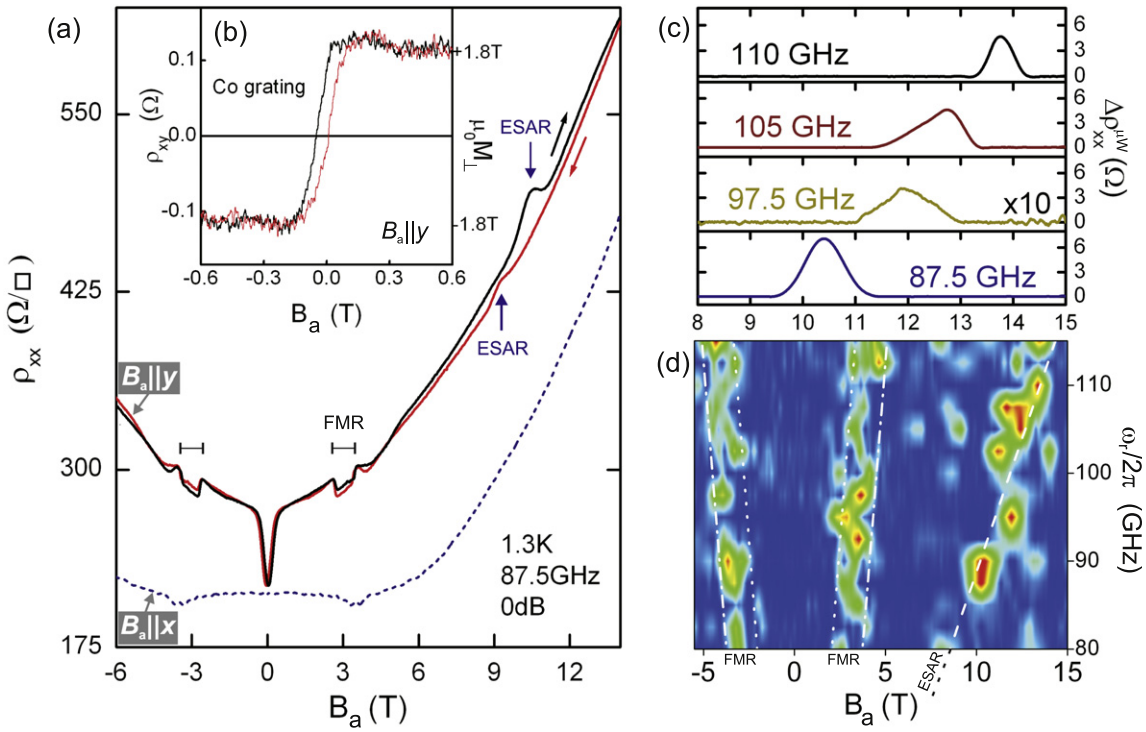

Figure 27. (a) Magnetoresistance of the cobalt superlattice of figure 26(a) irradiated by microwaves. The magnetic field B_a magnetizes the grating along the short axis of the stripes to apply the magnetic modulation (full lines) or along the long axis to switch it off (dashed lines). The electron spin anti-resonance (ESAR) peak is observed when both the magnetic modulation and the microwaves are applied. (b) The magnetization curve of the grating measured by Hall magnetometry; (c) frequency dependence of the ESAR peak; (d) ESAR and FMR peak amplitudes mapped as a function of magnetic field and microwave frequency.

The microwave induced resistance is obtained by writing the longitudinal conductivity as the sum of a conductivity component due to snake orbits which are free to propagate $\sigma_s(1 - P_{dark})$ and a conductivity component Σ due to other states. The Drude conductivity is $\sigma_0 = \sigma_s + \Sigma$. The change in longitudinal resistance brought about by the formation of the dark state is simply written as

$$(\rho_{xx} - \rho_0)/\rho_0 = \rho_0 \sigma_s P_{dark}. \tag{35}$$

Coherent population trapping increases the resistance proportionally to the probability of the dark state.

Figure 27(a) shows the magnetoresistance of the cobalt superlattice measured under microwave irradiation. The plot compares the effect of having the magnetic modulation ON (full lines) and OFF (dashed lines). We focus on the microwave induced features labelled FMR and ESAR (electron spin anti-resonance). The former is the ferromagnetic resonance of the cobalt grating detected by the 2DEG. The latter corresponds to the blockade of spin flips in snake orbits when the microwaves are tuned to the Zeeman energy—hence the term anti-resonance. The V-shaped magnetoresistance at low magnetic field is due to the magnetization of the cobalt grating.

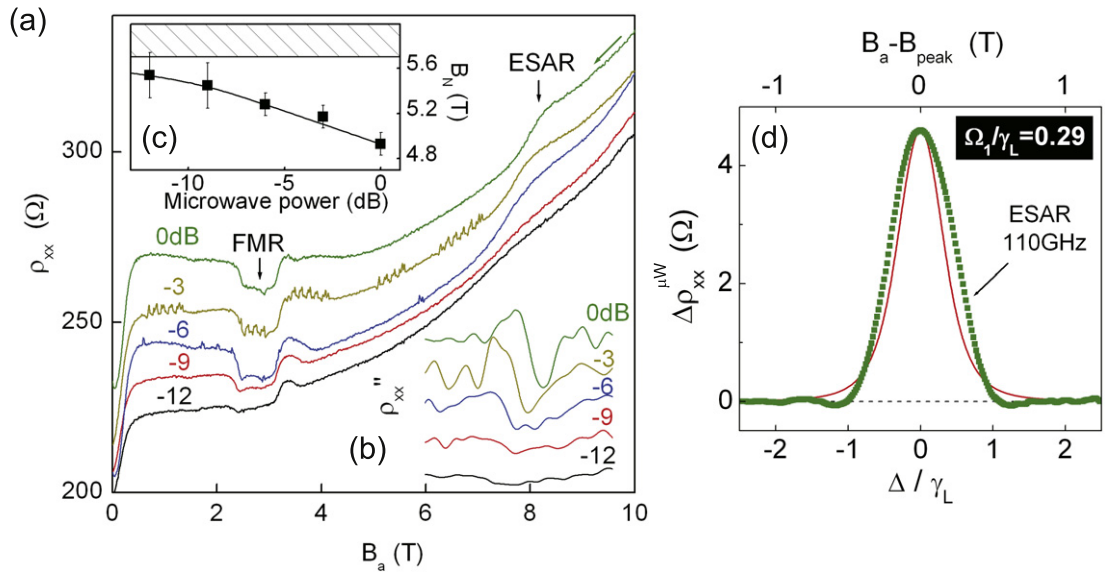

Figure 28. (a) Dependence of the magnetoresistance on microwave power; (b) second derivative of the magnetoresistance at the ESAR peak; (c) position of the ESAR peak plotted as a function of microwave power; (d) ESAR peak fitted with the theory described in the text.

From its amplitude we estimate the strength of the magnetic modulation as $\tilde{B}_1 = 0.141$ T in agreement with the value calculated from equation (1). The frequency dependence of the ESAR peak is shown in panel (c). Panel (d) maps the microwave induced change in resistance as a function of magnetic field and frequency. The FMR and ESAR shift to higher magnetic field at different rates as a function of ω_r. This accounts for the different Landé g-factors in cobalt and GaAs. The Landé g-factor of ESAR is $g = 0.43$ in agreement with the Landé g-factor of a GaAs quantum well when the magnetic field is applied in the plane. The Landé g-factor of FMR is $g = 1.8$. The temperature dependence shows that the ESAR peak vanishes at 40 K. The thermal activation plot also gives an activation energy corresponding to the Zeeman gap of GaAs. From this we extract the Landé g-factor of the 2DEG as $g = 0.40$. When the magnetic modulation is switched off (dashed lines) in panel (a), the ESAR peak vanishes. This suggests that ESAR differs from ESR. The non-observation of ESR in the dashed curve is not surprising because the 2D density of states is constant. Hence spin flips do not induce a change in the overall resistance. For ESR to be detected electrically, spin up and spin down subbands must have different conductivities. This situation is typically obtained at odd filling factors in quantum Hall systems but not here. The lack of ESR peak in the magnetoresistance is totally expected. The ESAR peak, however, is a new phenomenon induced by the combination of microwaves and the magnetic modulation.

The power dependence of the ESAR peak is shown in figure 28(a). The FMR line is independent of microwave power. By contrast the ESAR line, whose position is shown by the minimum in the second derivative curves of figure 28(b), appears to shift to higher magnetic field with increasing microwave power. This effect is related to a large shift of the ESAR line to lower magnetic field in figure 27(d). Extrapolating the ESAR to $\omega_r = 0$ demonstrates an internal magnetic field $B_N = 4.9$ T. This shift, known as the Overhauser effect, arises from the hyperpolarization of nuclear spins by electron spins during spin resonance [82]. Electron and nuclear spins are coupled through hyperfine interaction and, in their ground state, are parallel to each other—the electron charge and Landé factor being both negative. Electron spin resonance tends to equalize spin populations, which has the effect of predominantly flipping spins from up to down. Flip-flop processes increase the nuclear polarization to $\langle I_z \rangle = (\gamma_e/\gamma_n)\langle I_z \rangle_{\text{thermal}}$. The spin polarization is negative (antiparallel to the external field) and generates a nuclear magnetic field $B_N = b_n \langle I_z \rangle$ where the coefficient b_n calculated for different magnetic isotopes [83] is negative. This explains that B_N augments B_a shifting the ESAR line to lower magnetic field. B_N effectively measures the polarization of the nuclear spin system. In inset (b), B_N *decreases* with increasing microwave power demonstrating the decrease of the nuclear polarization. We extract B_N from the minimum in the second derivative and plot B_N as a function of microwave power in inset (c). The nuclear magnetization saturates at vanishing microwave power at $B_N = 5.6$ T. The saturation field theoretically predicted by Paget *et al* [83] is 5.3 T. The saturation of B_N at vanishing power can be explained by assuming that snake oscillators (not microwaves) dynamically polarize nuclei. This process is efficient because of extremely fast spin flips compared to the spin relaxation rate. Hyperfine interaction is comparable to that calculated by Paget *et al* for shallow impurities because the oscillator wavefunction is localized (on the line of zero magnetic field) and overlaps nuclei locally. Increasing microwave power *decreases* the Overhauser shift. This is the opposite of what one normally observes in conventional spin resonance. But this is totally consistent with the dark state blocking spin flips as the microwave power increases.

Figure 28(d) shows the experimental peak fitted with equations (34) and (35). We calculate $\tilde{\Omega}_1/(2\pi) = 0.81$ GHz and obtain the following values from the fit: $\Omega_r/(2\pi) \approx$

70 MHz and $\gamma_L = \gamma_T = 1.76 \times 10^{10}$ s^{-1}. The coefficient $\rho\sigma_s \approx 10$ is obtained from the positive magnetoresistance of snake orbits in figure 4. These results support coherent population trapping as the explanation for both the decrease in nuclear polarization with increasing microwave power and for the ESAR peak. The Rabi frequency of snake oscillators is close to the collisional broadening: $\Omega_1 = 0.29\gamma_L$. The huge Rabi frequencies of magnetic modulations thus enable coherent manipulation of the electron spin.

6. Prospects

The use of fringing magnetic fields opens device applications in magnetoelectronics and spintronics. For instance, micromagnets that apply a local magnetic field to HEMT structures will generate a local Hall voltage. Non-volatile memories operating on this principle have been demonstrated by Monzon *et al* [84] and Johnson *et al* [85]. Magnetic field sensors that use hybrid Hall junctions in the diffusive regime have also been studied both experimentally [86] and theoretically [87, 88]. The response of the Hall sensor was found to be independent of the functional shape of the magnetic field. The Hall resistance was however found to saturate due to the quasi-localization of electrons in the magnetic region. The channelling magnetoresistance is equally attractive for applications as it was shown to subsist at room temperature [60]. In particular, the dependence of the snake orbit magnetoresistance on the direction of the magnetic field can be used for making directional sensors of magnetic field.

Canted magnetic fields are useful in spintronics for spin filtering [61, 62, 75]. The inter-dependence of the orbital and spin dynamics presents exciting possibilities for inducing spin resonance with a direct current. This paves the way towards coherently controlling the electron spins with timed current pulses. This approach eliminates the need for cumbersome microwave apparatus. The inter-dependence works the other way round since a perturbation to the spin dynamics was shown to induce changes in the resistance. The coupling of the electron spin to its environment was studied with particular emphasis on the advantages derived from extremely fast Rabi oscillations. The coupling to the electromagnetic field yields weak microwave fluorescence. Hyperfine coupling of electron spins to atomic nuclei dynamically polarizes atomic nuclei on the drift path of snake orbits. In this way, electrically induced ESR may be used to initialize nuclear magnetic moments that represent quantum bits. At a more fundamental level, the fringing magnetic fields may help realize two-dimensional magnets modulated by a gradient of magnetic field. This system supports the formation of spin helices and quantized spin currents hypothesized by Haldane and Arovas [89, 90], which remain to be demonstrated.

Acknowledgments

The support of the EPSRC (EP/E002390) is gratefully acknowledged. I would also like to express my thanks to the following people who have granted me permission to reproduce their figures in this review article: D Frustaglia, B L Gallagher, W Hansen, T Heinzel, Y Iye, A Matulis, F M Peeters and J Wrobel.

Appendix. Stray magnetic field of stripes and dots

A.1. Stripe of rectangular cross section

Consider one of the finger gates in the grating of figure 1(a). This has width d, height h, magnetization (M_x, M_y, M_z) and is infinitely long. The stray magnetic field induced by the M_z component is

$$\begin{aligned} B_x^{(z)}(x, z_0) &= \frac{\mu_0 M_z}{2\pi}\{f(x, z, a, c) - f(x, z, a, -c)\} \\ B_y^{(z)}(x, z_0) &= 0 \\ B_z^{(z)}(x, z_0) &= \frac{\mu_0 M_z}{2\pi}\{g(x, z, a, c) - g(x, z, a, -c)\}. \end{aligned} \tag{36}$$

Similarly the stray field induced by the M_x component is

$$\begin{aligned} B_x^{(x)}(x, z_0) &= \frac{\mu_0 M_x}{2\pi}\{g(z, x, c, a) - g(z, x, c, -a)\} \\ B_y^{(x)}(x, z_0) &= 0 \\ B_z^{(x)}(x, z_0) &= \frac{\mu_0 M_x}{2\pi}\{f(z, x, c, a) - f(z, x, c, -a)\} \end{aligned} \tag{37}$$

where $f(\chi, \zeta, \alpha, \gamma) = \ln[\sqrt{\frac{(\chi+\alpha)^2+(\zeta-\gamma)^2}{(\chi-\alpha)^2+(\zeta-\gamma)^2}}]$ and $g(\chi, \zeta, \alpha, \gamma) = \arctan(\frac{\chi+\alpha}{\zeta-\gamma}) - \arctan(\frac{\chi-\alpha}{\zeta-\gamma})$. $a = d/2, c = h/2, z = -c - z_0$. The total fringing field is $B_\xi = B_\xi^{(x)} + B_\xi^{(z)}$ $(\xi = x, y, z)$.

A.2. Cylinder

Consider the ferromagnetic dot of figure 12. This is a cylinder of height h, radius a with magnetization $(0, 0, M_z)$. The stray magnetic field in this case is given by

$$B_z(x, z_0) = \frac{\mu_0 M_z}{2}\int_0^\infty \mathrm{d}(a\varepsilon) J_1(\varepsilon a) J_0(\varepsilon x) \mathrm{e}^{-\varepsilon z_0}[\mathrm{e}^{-\varepsilon h} - 1], \tag{38}$$

where J_0 and J_1 are the Bessel functions of the first kind.

References

[1] Lee D K K, Chalker J T and Ko D Y K 1994 Localization in a random magnetic field: the semiclassical limit *Phys. Rev.* B **50** 5272
[2] Yakubo K and Goto Y 1996 Localization of two-dimensional electrons in a random magnetic field *Phys. Rev.* B **54** 13432
[3] Sugiyama T and Nagaosa N 1993 Localization in a random magnetic field *Phys. Rev. Lett.* **70** 1980
[4] Zhang S C and Arovas D P 1994 Effective field theory of electron motion in the presence of random magnetic flux *Phys. Rev. Lett.* **72** 1886
[5] Müller J E 1992 Effect of a nonuniform magnetic field on a two-dimensional electron gas in the ballistic regime *Phys. Rev. Lett.* **68** 385
[6] Sheng D N and Weng Z Y 1995 Delocalization in a random magnetic field *Phys. Rev. Lett.* **75** 2388
[7] Avishai Y, Hatsugai Y and Kohmoto M 1993 Localization problem of a two-dimensional lattice in a random magnetic field *Phys. Rev.* B **47** 9561
[8] Xie X C, Wang X R and Liu D Z 1998 Kosterlitz–Thouless-type metal–insulator transition of a 2D electron gas in a random magnetic field *Phys. Rev. Lett.* **80** 3563

[9] Mirlin A D, Polyakov D G and Wölfle P 1998 Composite fermions in a long-range random magnetic field: Quantum Hall effect versus Shubnikov–de Haas oscillations *Phys. Rev. Lett.* **80** 2429

[10] Mancoff F B, Clarke R M, Marcus C M, Zhang S C, Campman K and Gossard A C 1995 Magnetotransport of a two-dimensional electron gas in a spatially random magnetic field *Phys. Rev.* B **51** 13269

[11] Magier R and Bergman D J 2006 Strong field magnetotransport of two-phase disordered media in two and three dimensions: exact and approximate results *Phys. Rev.* B **74** 094423

[12] Bending S J, von Klitzing K and Ploog K 1990 Two-dimensional electron gases as a flux detector for a type II superconducting film *Phys. Rev.* B **42** 9859

[13] Geim A K, Bending S J and Grigorieva I V 1992 Asymmetric scattering and diffraction of two-dimensional electrons at quantized tubes of magnetic flux *Phys. Rev. Lett.* **69** 2252

[14] Craik D 1997 *Magnetism Principles and Applications* (New York: Wiley)

[15] Gerhardts R R 1996 Quasiclassical calculation of magnetoresistance oscillations of a two-dimensional electron gas in spatially periodic magnetic and electrostatic fields *Phys. Rev.* B **53** 11064

[16] Nogaret A, Overend N, Gallagher B L, Main P C, Henini M, Marrows C H, Howson M A and Beaumont S P 1998 Giant magnetoresistance and hysteretic effects in hybrid semiconductor/ferromagnet devices *Physica* E **2** 421

[17] Nogaret A, Carlton S, Gallagher B L, Main P C, Henini M, Wirtz R, Newbury R, Howson M A and Beaumont S P 1997 Observation of giant magnetoresistance due to open orbits in hybrid semiconductor/ferromagnet devices *Phys. Rev.* B **55** 16037

[18] Matulis A, Peeters F M and Vasilopoulos P 1994 Wave-vector-dependent tunneling through magnetic barriers *Phys. Rev. Lett.* **72** 1518

[19] Leadbeater M L, Foden C L, Burroughes J H and Pepper M 1995 Magnetotransport in a nonplanar two-dimensional electron gas *Phys. Rev.* B **52** R8629

[20] Gusev G M, Gennser U, Kleber X, Maude D K, Portal J C, Lubyshev D I, Basmaji P, de P A Silva M, Rossi J C and Nastaushev Yu V 1996 Quantum interference effects in a strongly fluctuating magnetic field *Phys. Rev.* B **53** 13641

[21] Grayson M, Schuh D, Bichler M, Huber M, Abstreiter G, Hoeppel L, Smet J and von Klitzing K 2004 Quantum Hall effect in a two-dimensional electron gas bent by 90 degrees *Physica* E **22** 181

[22] Mendach S, Schumacher O, Welsch H, Heyn Ch, Hansen W and Holz M 2006 Evenly curved two-dimensional electron systems rolled-up Hall bars *Appl. Phys. Lett.* **88** 212113

[23] Foden C l, Leadbeater M L, Burroughes J H and Pepper M 1994 Quantum magnetic confinement in a curved two-dimensional electron gas *J. Phys.: Condens. Matter* **6** L127

[24] Smet J H, von Klitzing K, Weiss D and Wegscheider W 1998 dc transport of composite fermions in weak periodic potentials *Phys. Rev. Lett.* **80** 4538

[25] Smet J H, Jobst S, von Klitzing K, Weiss D, Wegscheider W and Umansky V 1999 Commensurate composite fermions in weak periodic electrostatic potentials: direct evidence of a periodic effective magnetic field *Phys. Rev. Lett.* **83** 2620

[26] Carmona H A, Geim A K, Nogaret A, Main P C, Foster T J and Henini M 1995 Two-dimensional electrons in a lateral magnetic superlattice *Phys. Rev. Lett.* **74** 3009

[27] Ye P D, Weiss D, Gerhardts R R, von Klitzing K, Eberl K, Nickel H and Foxon C T 1995 Strain-induced magnetoresistance oscillations in GaAs–AlGaAs heterojunctions with ferromagnetic and superconducting submicrometre gratings *Semicond. Sci. Technol.* **10** 715

[28] Ye P D, Weiss D, Gerhardts R R, Seeger M, von Klitzing K, Eberl K and Nickel H 1995 Electrons in a periodic magnetic field induced by an array of micromagnets *Phys. Rev. Lett.* **74** 3013

[29] Izawa S, Katsumoto S, Endo A and Iye Y 1995 Magnetoresistance oscillations in two-dimensional electron gas under spatially modulated vector potential *J. Phys. Soc. Japan* **64** 706

[30] Peeters F M and Vasilopoulos P 1993 Quantum transport of a two-dimensional electron gas in a spatially modulated magnetic field *Phys. Rev.* B **47** 1466

[31] Beenakker C W J 1989 Guiding-center-drift resonance in a periodically modulated two-dimensional electron gas *Phys. Rev. Lett.* **62** 2020

[32] Gornyi I V and Mirlin A D 2004 Interaction-induced magnetoresistance in a two-dimensional electron gas *Phys. Rev.* B **69** 045313

[33] Evers F, Mirlin A D and Polyakov D G 1999 Semiclassical theory of transport in a random magnetic field *Phys. Rev.* B **60** 8951

[34] Overend N, Nogaret A, Gallagher B L, Main P C, Henini M, Marrows C H, Howson M A and Beaumont S P 1998 Temperature dependence of large positive magnetoresistance in hybrid ferromagnetic/semiconductor devices *Appl. Phys. Lett.* **72** 1724

[35] Nogaret A, Bending S J and Henini M 2000 Resistance resonance effects through magnetic edge states *Phys. Rev. Lett.* **84** 2231

[36] Nogaret A, Lawton D N, Maude D K, Portal J C and Henini M 2003 Hall anomaly of diffusive magnetic waveguides *Phys. Rev.* B **67** 165317

[37] Lawton D N, Nogaret A, Bending S J, Maude D K, Portal J C and Henini M 2001 Suppression of magnetic channelling in microscopic magnetic waveguides *Phys. Rev.* B **64** 033312

[38] Reijniers J and Peeters F M 2001 Resistance effects due to magnetic guiding orbits *Phys. Rev.* B **63** 165317

[39] Fleischmann R, Geisel T and Ketzmerick R 1992 Magnetoresistance due to chaos and nonlinear resonances in lateral surface superlattices *Phys. Rev. Lett.* **68** 1367

[40] Ye P D, Weiss K, von Klitzing K, Eberl K and Nickel H 1995 Fabrication and characterization of micromagent arrays on top of GaAs/AlGaAs heterostructures *Appl. Phys. Lett.* **67** 1441

[41] Eroms J, Tolkiehn M, Weiss D, Rössler U, De Boeck J and Borghs G 2002 Commensurability effects in Andreev antidot billiards *Europhys. Lett.* **58** 569

[42] Uzur D, Nogaret A, Beere H E, Ritchie D A, Marrows C H and Hickey B J 2004 Probing the annular electronic shell structure of a magnetic corral *Phys. Rev.* B **69** 241301

[43] Kocsis B, Palla G and Cserti J 2005 Quantum and semiclassical study of magnetic dots *Phys. Rev.* B **71** 075331

[44] Sim H-S, Ihm G, Kim N and Chang K J 2001 Magnetic quantum dot: a magnetic transmission barrier and resonator *Phys. Rev. Lett.* **87** 146601

[45] Reijniers J, Peeters F M and Matulis A 2001 Electron scattering on circular symmetric magnetic field profiles in a two-dimensional electron gas *Phys. Rev.* B **64** 245314

[46] Ibrahim I S and Peeters F M 1995 Two-dimensional electrons in lateral magnetic superlattices *Phys. Rev.* B **54** 17321

[47] Yang X-D, Wang R-Z, Guo Y, Yang W, Yu D-B, Wang B and Yan H 2004 Giant magnetoresistance effect of two-dimensional electron gas systems in a periodically modulated magnetic field *Phys. Rev.* B **70** 115303

[48] Peeters F M and Matulis A 1993 Quantum structures created by nonhomogeneous magnetic fields *Phys. Rev.* B **48** 15166

[49] Krakovsky A 1996 Electronic band structure in a periodic magnetic field *Phys. Rev.* B **53** 8469

[50] Reijniers J, Matulis A, Chang K, Peeters F M and Vasilopoulos P 2002 Confined magnetic guiding orbit states *Europhys. Lett.* **59** 749

[51] Chang M C and Niu Q 1994 Electron band structure in a two-dimensional periodic magnetic field *Phys. Rev.* B **50** 10843

[52] Nogaret A, Portal J-C, Beere H E, Ritchie D A and Phillips C 2009 Quantum interferences of magnetic edge channels activated by intersubband optical transitions in magnetically confined quantum wires *J. Phys.: Condens. Matter* **21** 025303

[53] Edmonds K W, Gallagher B L, Main P C, Overend N, Wirtz R, Nogaret A, Henini M, Marrows C H, Hickey B J and Thoms S 2001 Magnetoresistance oscillations due to the internal Landau band structure of a two-dimensional electron system in a periodic magnetic field *Phys. Rev.* B **64** 041303

[54] Shi J, Peeters F M, Edmonds K W and Gallagher B L 2002 Even-odd transition in the Shubnikov–de Haas oscillations in a two-dimensional electron gas subjected to a periodic magnetic and electric modulations *Phys. Rev.* B **66** 035328

[55] Hara M, Endo A, Katsumoto S and Iye Y 2004 Transport in a two-dimensional electron-gas narrow channel with a magnetic-field gradient *Phys. Rev.* B **69** 153304

[56] Lawton D, Nogaret A, Makarenko M V, Kibis O V, Bending S J and Henini M 2002 Electrical rectification by magnetic edge states *Physica* E **13** 699

[57] Governale M and Boese D 2000 Magnetic barrier in confined two-dimensional electron gases: nanomagnetometers and magnetic switches *Appl. Phys. Lett.* **77** 3215

[58] Song J-F, Bird J P and Ochai Y 2005 Manipulating the transmission of a two-dimensional electron gas via spatially varying magnetic fields *Appl. Phys. Lett.* **86** 062106

[59] Ibrahim I S, Schweigert V A and Peeters F M 1997 Classical transport of electrons through magnetic barriers *Phys. Rev.* B **56** 7508

[60] Kubrak V, Rahman F, Gallagher B L, Main P C, Henini M, Marrows C H and Howson M A 1999 Magnetoresistance of a two-dimensional electron gas due to a single barrier and its use for nanomagnetometry *Appl. Phys. Lett.* **74** 2507

[61] Bae J-U, Lin T-Y, Yoon Y, Kim S J, Imre A, Porod W, Reno J L and Bird J P 2008 Large tunneling magnetoresistance in a field effect transistor with a nanoscale ferromagnetic gate *Appl. Phys. Lett.* **92** 253101

[62] Lin T-Y, Bae J-U, Bohra G, Lim K, Reno J L and Bird J P 2009 Influence of quantum-interference on the fringing-field magnetoresistance of hybrid ferromagnetic/semiconductor devices *Appl. Phys. Lett.* **95** 143113

[63] Vančura T, Ihn T, Broderick S, Ensslin K, Wegscheider W and Bichler M 2000 Electron transport in a two-dimensional electron gas with magnetic barriers *Phys. Rev.* B **62** 5074

[64] Cerchez M, Hugger S, Heinzel T and Schulz N 2007 Effect of edge transmission and elastic scattering on the resistance of magnetic barriers: experiment and theory *Phys. Rev.* B **75** 035341

[65] Ismail K, Antoniadis D A and Smith H D 1989 Lateral resonant tunneling in a double-barrier field-effect transistor *Appl. Phys. Lett.* **55** 589

[66] De Martino A, Dell'Anna L and Egger R 2007 Magnetic confinement of massless Dirac fermions in graphene *Phys. Rev. Lett.* **98** 066802

[67] Park S and Sim H-S 2008 Magnetic egde states in graphene in nonuniform magnetic fields *Phys. Rev.* B **77** 075433

[68] Ramezani Masir M, Vasilopoulos P and Peeters F M 2009 Magnetic Kronig–Penney model for Dirac electrons in single-layer graphene *New J. Phys.* **11** 095009

[69] Dell'Anna L and De Martino A 2009 Multiple magnetic barriers in graphene *Phys. Rev.* B **79** 045420

[70] Xu H, Heinzel T, Evaldsson M and Zozoulenko I V 2008 Magnetic barriers in graphene nanoribbons: theoretical study of transport properties *Phys. Rev.* B **77** 245401

[71] Pioro-Ladrière M, Obata T, Tokura Y, Shin Y-S, Kubo T, Yoshida K, Taniyama T and Tarucha S 2008 Electrically driven single-electron spin resonance in a slanting Zeeman field *Nat. Phys.* **4** 776

[72] Nogaret A 2005 Electrically induced Raman emission from planar spin oscillator *Phys. Rev. Lett.* **94** 147207

[73] Nogaret A and Peeters F M 2007 Electrically induced spin resonance fluorescence. I. Theory *Phys. Rev.* B **76** 075311

[74] Nogaret A, Lambert N J and Peeters F M 2007 Electrically induced spin resonance fluorescence. II. Fluorescence spectra *Phys. Rev.* B **76** 075312

[75] Wróbel J, Dietl T, Łusakowski A, Grabecki G, Fronc K, Hey R, Ploog K H and Shtrikman H 2004 Spin filtering in a hybrid ferromagnetic–semiconductor microstructure *Phys. Rev. Lett.* **93** 246601

[76] Nitta J and Bergsten T 2007 Time reversal Aharonov–Casher effect using Rashba spin–orbit interaction *New J. Phys.* **9** 341

[77] Frustaglia D, Hentschel M and Richter K 2001 Quantum transport in nonuniform magnetic fields: Aharonov–Bohm ring as a spin switch *Phys. Rev. Lett.* **87** 256602

[78] Frustaglia D and Richter K 2004 Spin interference in ring conductors subject to Rashba coupling *Phys. Rev.* B **69** 235310

[79] Frustaglia D, Hentschel M and Richter K 2004 Aharonov–Bohm physics with spin. II. Spin flip effects in two-dimensional ballistic systems *Phys. Rev.* B **69** 155327

[80] Nogaret A, Samardak S and Peeters F 2008 High harmonic generation from spin resonance fluorescence *Physica* E **40** 1223

[81] Fleischauer M, Imamoglu A and Marangos J P 2005 Electromagnetically induced transparency: optics in coherent media *Rev. Mod. Phys.* **77** 633

[82] Abragam A 2004 *Principles of Nuclear Magnetism* (Oxford: Oxford University Press)

[83] Paget D, Lampel G, Sapoval B and Safarov V I 1977 Low field electron-nuclear spin coupling in gallium arsenide under optical pumping conditions *Phys. Rev.* B **15** 5780

[84] Monzon F G, Johnson M and Roukes M L 1997 Strong Hall voltage modulation in hybrid ferromagnet/semiconductor microstructures *Appl. Phys. Lett.* **71** 3087

[85] Johnson M, Bennett B R, Yang M J, Miller M M and Shanabrook B V 1997 Hybrid Hall effect device *Appl. Phys. Lett.* **71** 974

[86] Novoselov K S, Geim A K, Dubonos S V, Cornelissens Y G, Peeters F M and Mann J C 2002 *Phys. Rev.* B **65** 233312

[87] Ibrahim I S, Schweigert V A and Peeters F M 1998 Diffusive transport in a Hall junction with a microinhomogeneous magnetic field *Phys. Rev.* B **57** 15416

[88] Cornelissens Y G and Peeters F M 2002 Response function of a Hall magnetosensor in the diffusive regime *J. Appl. Phys.* **92** 2006

[89] Haldane F D M and Arovas D P 1995 Quantized spin currents in two-dimensional magnets *Phys. Rev.* B **52** 4223

[90] Wen X G, Wilczek F and Zee A 1989 Chiral spin states and superconductivity *Phys. Rev.* B **39** 11413